nature cancer

Resource

https://doi.org/10.1038/s43018-023-00566-3

Phenotypic diversity of T cells in human primary and metastatic brain tumors revealed by multiomic interrogation

Received: 30 September 2022

Accepted: 19 April 2023

Published online: 22 May 2023

Check for updates

Vladimir Wischnewski[1,2,3,4], Roeltje R. Maas[1,2,3,4,5,6,14], Paola Guerrero Aruffo[1,2,3,4,14], Klara Soukup[1,2,3,14], Giovanni Galletti[7], Mara Kornete[1,2], Sabine Galland[1,2,3,4,8], Nadine Fournier[3,9], Johanna Lilja[1,2,3], Pratyaksha Wirapati[3,9], Joao Lourenco[9], Alice Scarpa[7], Roy T. Daniel[4,6], Andreas F. Hottinger[4,8], Jean-Philippe Brouland[10], Agnese Losurdo[11], Emanuele Voulaz[12,13], Marco Alloisio[12,13], Monika E. Hegi[4,5,6], Enrico Lugli[7] & Johanna A. Joyce[1,2,3,4] ✉

The immune-specialized environment of the healthy brain is tightly regulated to prevent excessive neuroinflammation. However, after cancer development, a tissue-specific conflict between brain-preserving immune suppression and tumor-directed immune activation may ensue. To interrogate potential roles of T cells in this process, we profiled these cells from individuals with primary or metastatic brain cancers via integrated analyses on the single-cell and bulk population levels. Our analysis revealed similarities and differences in T cell biology between individuals, with the most pronounced differences observed in a subgroup of individuals with brain metastasis, characterized by accumulation of *CXCL13*-expressing CD39^{+} potentially tumor-reactive T (pTRT) cells. In this subgroup, high pTRT cell abundance was comparable to that in primary lung cancer, whereas all other brain tumors had low levels, similar to primary breast cancer. These findings indicate that T cell-mediated tumor reactivity can occur in certain brain metastases and may inform stratification for treatment with immunotherapy.

Malignancies in the brain are subdivided into primary tumors arising within this tissue, such as gliomas, and tumors of extracranial origin that subsequently metastasize to the brain[1]. Primary tumors most frequently associated with the development of brain metastasis (BrM) include lung, melanoma and breast cancers (BCs)[2]. Despite improvements in tumor detection and local treatment and the introduction of new therapies, including molecular-targeted and immune-based approaches, the prognosis for individuals diagnosed with aggressive

[1]Department of Oncology, University of Lausanne, Lausanne, Switzerland. [2]Ludwig Institute for Cancer Research, University of Lausanne, Lausanne, Switzerland. [3]Agora Cancer Research Centre Lausanne, Lausanne, Switzerland. [4]Lundin Family Brain Tumor Research Center, Departments of Oncology and Clinical Neurosciences, Centre Hospitalier Universitaire Vaudois, Lausanne, Switzerland. [5]Neuroscience Research Center, Centre Hospitalier Universitaire Vaudois, Lausanne, Switzerland. [6]Department of Neurosurgery, Centre Hospitalier Universitaire Vaudois, Lausanne, Switzerland. [7]Laboratory of Translational Immunology, IRCCS Humanitas Research Hospital, Milan, Italy. [8]Department of Oncology, Centre Hospitalier Universitaire Vaudois, Lausanne, Switzerland. [9]Translational Data Science, Swiss Institute of Bioinformatics, Lausanne, Switzerland. [10]Department of Pathology, Centre Hospitalier Universitaire Vaudois, Lausanne, Switzerland. [11]Oncology Department, IRCCS Humanitas Research Hospital, Milan, Italy. [12]Department of Biomedical Sciences, Humanitas University, Milan, Italy. [13]Division of Thoracic Surgery, IRCCS Humanitas Research Hospital, Milan, Italy. [14]These authors contributed equally: Roeltje R. Maas, Paola Guerrero Aruffo, Klara Soukup. ✉e-mail: johanna.joyce@unil.ch

brain cancer remains poor, with estimated 2-year survival rates of <20% (refs. 2–4), underscoring the need to better understand this disease as a means to develop effective therapies.

Although cytotoxic T cells are generally excluded from healthy brain parenchyma to prevent excessive neuroinflammation under homeostatic conditions, the impairment of the blood–brain barrier in advanced brain malignancies can facilitate the infiltration of peripheral immune cells, including $CD8^+$ T cells[5,6]. The abundance of $CD8^+$ T cells, however, is heterogeneous and typically higher in BrM than in gliomas[5,7]. Several clinical trials assessing the efficacy of immune checkpoint blockade (ICB) to target T cells have shown some intracranial responses in small subgroups of individuals with melanoma[8] and lung[9] cancer with BrM but have largely failed in individuals with high-grade gliomas[10].

The heterogeneous efficacy of ICB in individuals with intracranial, but also extracranial, tumors has resulted in substantial efforts to identify biomarkers that would reliably predict response to this treatment. Together with tumor-intrinsic factors, including mismatch repair deficiency[11] and mutational burden[12], the presence of $CD8^+$ tumor-infiltrating lymphocytes (TILs) is associated with better response to ICB and prolonged overall survival in extracranial tumors[13,14] and BrM[15].

Given the considerable phenotypic diversity of $CD8^+$ T cells in tumors[16], several studies have sought to identify distinct subsets associated with, and responsible for, the response to ICB. Clonal expansion[17,18] and the expression of a distinct dysfunctional program in $CD8^+$ T cells correlated with better outcome in several cancer types[19–21]. Moreover, RNA expression of *CXCL13* by clonally expanded $CD8^+$ T cells with an exhaustion phenotype has emerged as a robust predictor for ICB efficacy across multiple tumor types[22–24]. Initial analyses have associated these $CD8^+$ T cell subsets with reactivity against a subset of tumor antigens, suggesting direct tumor reactivity[25]. The abundance of these potentially tumor-reactive T (pTRT) cells varies substantially across cancer types, which may influence ICB response[26]. Critically, whether pTRT cells can also infiltrate brain tumors and, if so, to what extent remain unknown.

To address this question, we performed a comprehensive analysis of circulating and tumor-infiltrating T cells in a large cohort of 84 individuals with brain cancer (36 with glioma and 48 with BrM) and 44 individuals with extracranial tumors (33 lung primary tumors and 11 breast primary tumors). Our analyses included single-cell and bulk RNA sequencing (RNA-seq), T cell antigen receptor (TCR) profiling, high-dimensional flow cytometry (FCM) and immunofluorescence (IF) spatial imaging and functional ex vivo assays. This multifaceted orthogonal strategy revealed that a subgroup of individuals with BrM, but not glioma, displayed substantial tumor infiltration with pTRT cells. Notably, most of these pTRT cell-high BrM arose from lung cancer and showed comparable pTRT cell abundance to primary lung cancer samples. Together, these results indicate that T cell-mediated tumor reactivity within the brain can occur, albeit in a subset of individuals with BrM.

Results

Single-cell RNA-seq identifies pTRT cells in individuals with BrM

To assess the extent of phenotypical and functional heterogeneity of T cells in individuals with brain cancers, specifically gliomas and BrM, we used an integrated analytical pipeline[27] to profile RNA and protein expression at the single-cell and bulk population levels (Extended Data Fig. 1a). We began by analyzing TILs and matched circulating T cells by single-cell RNA-seq (scRNA-seq) from six individuals with BrM and three individuals with glioma (Supplementary Table 1a and Extended Data Fig. 1b). Uniform manifold approximation and projection (UMAP) of 55,000 T cells in total showed substantial transcriptional differences between TILs and circulating T cells (Fig. 1a) and between $CD4^+$ and $CD8^+$ T cells (Fig. 1b). We identified 17 distinct clusters (Fig. 1c): seven $CD8^+$ T cell clusters (C1, C2, C3, C6, C7, C14 and C16) and eight $CD4^+$ T cell clusters (C0, C4, C5, C8, C9, C10, C11 and C13), with C4 representing regulatory T (T_{reg}) cells (Fig. 1c and Supplementary Table 1b). C12 and C15 contained both $CD4^+$ and $CD8^+$ T cells. Cryopreservation did not alter the composition and phenotype of T cell subpopulations (Extended Data Fig. 1c–e), consistent with a previous study[28].

Next, we compared cluster composition between individuals with glioma and BrM and found minimal variation in the blood (Fig. 1d and Extended Data Fig. 1f). By contrast, there were considerable differences in $CD8^+$ TIL composition in gliomas with a high abundance of C1 and in BrM samples with a high abundance of C3 (Fig. 1d and Extended Data Fig. 1f). To determine cluster-specific genes for all $CD8^+$ T cells, we performed differential expression analysis (DEA) and found that cells in C1 expressed *FTH1*, *CREM*, *GPR183*, *FOS* and *IL7R*, among other genes, but lacked expression of other activation markers, thereby suggesting an early activated state (Fig. 1e and Supplementary Table 1b)[29]. C3 was characterized by the expression of *CXCL13*, *RGS1*, *CTLA4*, *GZMB* and *IFNG* and multiple inhibitory receptors, indicating an overstimulated and dysfunctional phenotype (Fig. 1e and Supplementary Table 1b). Consequently, projection of our data onto a reference single-cell atlas of canonical T cell states[30] revealed that C1 contained predominantly early active and effector memory $CD8^+$ T cells, while cells in C3 primarily showed a precursor exhausted (T_{pex}) or exhausted (T_{ex}) phenotype (Extended Data Fig. 1g).

Because several studies have linked *CXCL13* expression and a dysfunctional state to tumor reactivity[16,22–26], we hypothesized that C3 contains tumor-specific $CD8^+$ T cells. We thus queried $CD8^+$ T cells for expression of previously defined gene signatures of neoantigen-reactive $CD8^+$ T cells[16,25,31–33] (Supplementary Table 1c) and indeed found the highest expression in C3 (Fig. 1f). Moreover, 42% of T cells in C3 were substantially expanded (containing large and hyperexpanded clonotypes) versus 11% in C1, suggesting higher clonality in C3 (Fig. 1g). Additionally, tumor-expanded clonotypes in C3 were largely absent from the blood, indicating local expansion within the tumor, while those in C1 were also detected in the circulation, suggesting brain tumor-unrelated specificity, such as against viral antigens (Fig. 1h). Indeed, seven TCR clonotypes in C1 could be matched

Fig. 1 | scRNA-seq identifies pTRT cells in a subset of individuals with BrM and defines a BrM pTRT cell-specific gene signature. a–**c**, UMAP of T cells from nine individuals with brain cancer colored by tissue (**a**), cell type (**b**) and cluster ID (**c**). **d**, Stacked bar plots showing the abundance of each cluster in blood and tumors, respectively, from individuals with BrM ($n = 6$) and glioma ($n = 3$). **e**, Expression heat map showing the top ten genes in each $CD8^+$ T cell cluster from $n = 9$ individuals. **f**, Enrichment of neoantigen-reactive $CD8^+$ T cell gene signatures in each $CD8^+$ T cell cluster, as indicated by the corresponding matched colors. The five different gene signatures analyzed are denoted by first author and year and can be found in the references. **g**, Stacked bar plot showing the clonality of the TCR in each $CD8^+$ T cell cluster. TCR clonotypes are grouped into five categories based on their prevalence in each individual and are colored accordingly; ND, not detected. **h**, Alluvial plots visualizing the frequency of the top 15 TCR clonotypes within C1 (left) and C3 (right), respectively. Each clonotype within one cluster is annotated with a unique color. **i**, Number of TCR clonotypes perfectly matched with published virus-specific TCRs from VDJdb in each $CD8^+$ T cell cluster from $n = 9$ individuals; CMV, cytomegalovirus; EBV, Epstein–Barr virus; HCV, hepatitis C virus. **j**, Abundance of C3 within each tumor. Samples are annotated as C3 high with a cumulative abundance of >30% (dotted horizontal line) or as C3 low. **k**, Dot plot showing average expression for each gene in $n = 5{,}188$ cells from C3 in C3-high tumors ($n = 3$ tumors) versus $n = 920$ cells from C3 in C3-low tumors ($n = 6$ tumors). Genes identified as DEGs in Seurat are highlighted. **l**, Bar plots showing the difference in abundance of defined T cell states in C3-high ($n = 3$ tumors) versus C3-low ($n = 3$ tumors) tumors depicted as fold change; Eff. Mem., effector memory; T_{FH}, follicular helper T cells; T_H1, type 1 helper T cells.

https://doi.org/10.1038/s43018-023-00566-3

to published TCR sequences with validated antiviral specificities, while none were found among cells in C3 (Fig. 1i and Supplementary Table 1d). Together, these findings indicate that C3 contains pTRT cells.

We next analyzed C3 abundance in each individual and found substantial heterogeneity (Fig. 1j). All gliomas and half of the BrM samples had comparably low levels of these cells (<15% of CD8$^+$ T cells) and were defined as C3 low, while the other half of BrM tumors were highly infiltrated with C3 cells (>30% of CD8$^+$ T cells) and were classified as C3 high (Fig. 1j). The abundance of cells within C3, as determined by scRNA-seq, positively correlated with total CD8$^+$ T cell frequencies acquired during

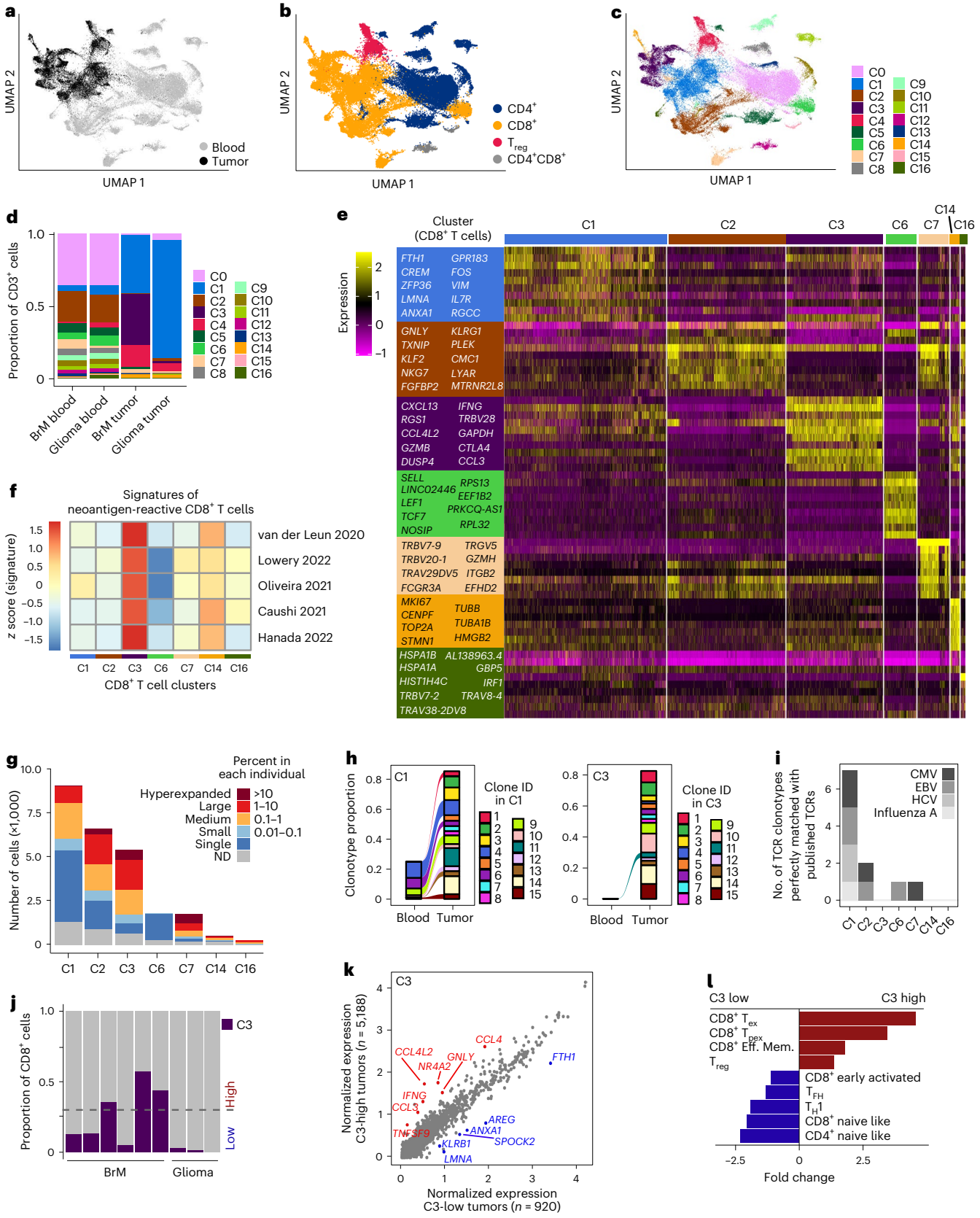

https://doi.org/10.1038/s43018-023-00566-3

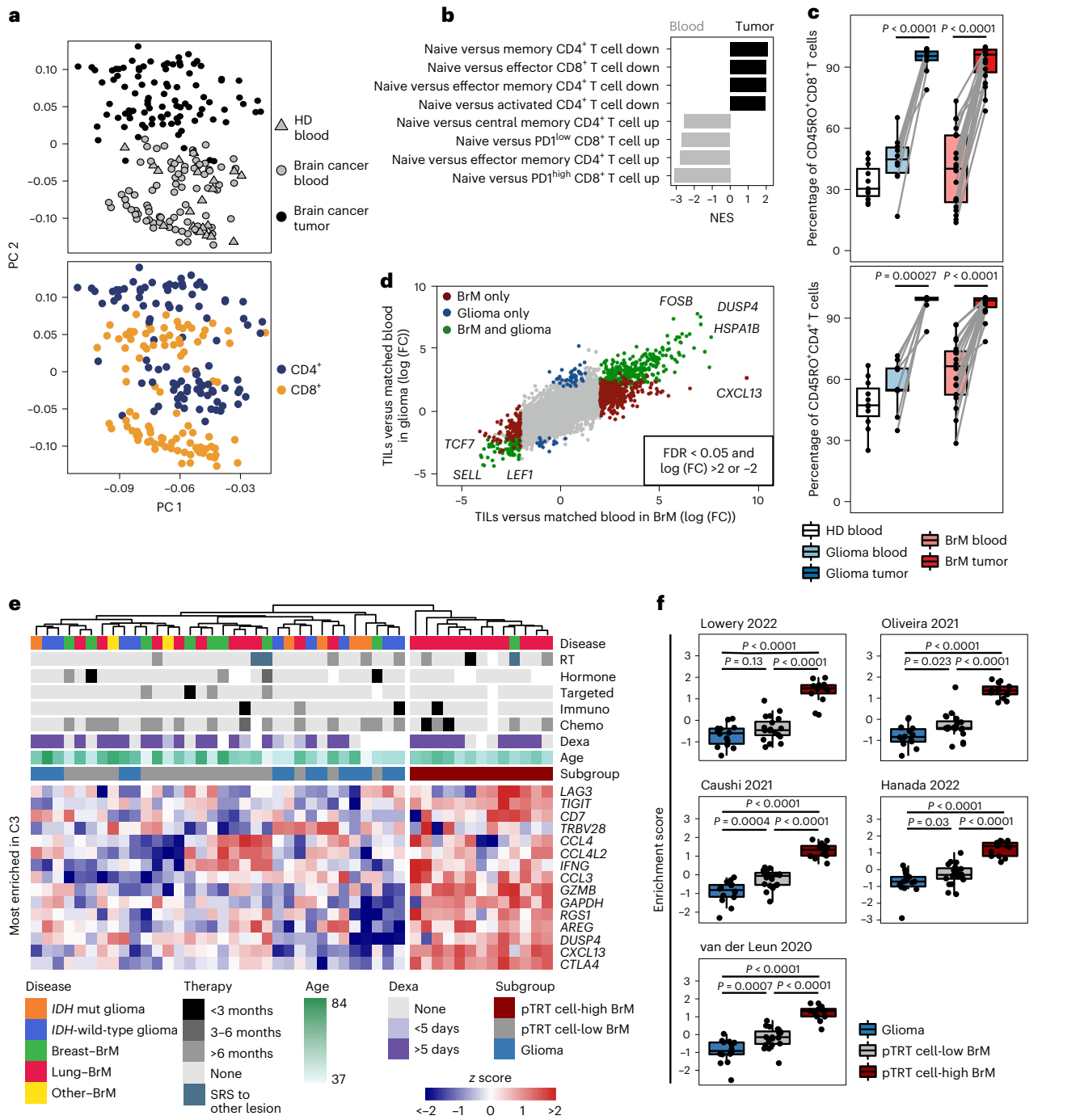

Fig. 2 | T cell activation and differentiation is a common feature of brain tumor-infiltrating T cells. a, Principal-component analysis based on the 250 most variably expressed genes (see Supplementary Table 2a for gene list) across all T cells (CD4$^+$ and CD8$^+$ from the blood and tumors) colored by tissue (top) or cell type (bottom) sorted from 54 individuals with brain cancer (tumor and blood) and blood from 12 HDs. For clinical details, see Supplementary Table 1a; PC, principal component. **b**, Bar plot showing GSEA of the comparison between T cells from blood ($n = 85$) and tumor ($n = 102$) samples using the MSigDB C7 collection filtered to contain only T cell-related pathways (see Supplementary Table 2b for full pathway list); NES, normalized enrichment score. **c**, Box plots representing the proportion of CD45RO$^+$ cells among CD8$^+$ (top) and CD4$^+$ (bottom) T cells in $n = 11$ HD, $n = 10$ glioma and $n = 19$ BrM blood samples, and $n = 9$ glioma and $n = 19$ BrM tumor samples. Matched brain cancer samples are denoted by connected lines. Significance was determined by paired two-sided Wilcoxon test. Box plots represent first and third quartiles with the medians as the center; whiskers show 1.5× the interquartile range of the 25th and 75th percentiles. **d**, Dot plot showing the fold change (FC) of each gene between matched blood and tumor CD8$^+$ T cells in $n = 33$ individuals with BrM (x axis) and $n = 14$ individuals with glioma (y axis). Genes passing the indicated significance cutoff in one or both diseases are colored as indicated. Most enriched shared genes in tumors or blood are highlighted, including *CXCL13* as the most DEG between glioma and BrM CD8$^+$ TILs; FDR, false discovery rate. **e**, Expression heat map and hierarchical clustering of top genes from C3 in CD8$^+$ T cells from $n = 47$ tumors in the bulk RNA-seq cohort. Columns and rows (z score) are hierarchically clustered. Disease and pTRT cell status are annotated per column; RT, radiotherapy; Hormone, hormone therapy; Targeted, targeted therapy; Immuno, immunotherapy; Chemo, chemotherapy; Dexa, dexamethasone; SRS, stereotactic radiosurgery. **f**, Box plots showing the enrichment of neoantigen-reactive CD8$^+$ T cell gene signatures in CD8$^+$ TILs in $n = 14$ individuals with glioma, $n = 20$ individuals with pTRT cell-low BrM and $n = 13$ individuals with pTRT cell-high BrM (five different signatures). Significance was determined with an unpaired two-sided Wilcoxon test and a Benjamini–Hochberg multiple comparison correction. Box plots are defined as in **c**.

cell sorting before single-cell encapsulation (Extended Data Fig. 1h). To investigate whether the phenotype of C3 cells also differed between these two groups, we performed DEA, which revealed that cells from C3-high tumors expressed higher levels of *TNFSF9*, *IFNG*, *GNLY*, *CCL3*, *CCL4* and *CCL4L2*, while those from C3-low samples showed higher expression of *FTH1*, *AREG* and *KLRB1*, among others. This suggested a more cytotoxic state of these cells in C3-high tumors (Fig. 1k).

Tumor-specific T cells can have different phenotypes, however, the majority show evidence of terminal exhaustion[31,33,34]. Comparison of canonical T cell states[30] in C3-high versus C3-low tumors revealed substantially higher proportions of T_{pex} and T_{ex} cell gene signatures in C3-high tumors, while naive T cell gene signatures were more enriched in C3-low samples (Fig. 1l). Taken together, our scRNA-seq analysis identified a subset of BrM tumors infiltrated with pTRT cells.

A subset of individuals with BrM show relatively high pTRT cell abundance

To expand our analyses beyond the 9 individuals in the scRNA-seq analysis, we next profiled a larger cohort, including TILs and matched blood T cells that were sorted from 54 individuals with brain cancer and the blood of 12 healthy donors (HDs), using population bulk RNA-seq (termed 'bulk RNA-seq cohort'; Supplementary Table 1a and Extended Data Fig. 2a). Principal-component analysis revealed the largest differences between TILs and circulating T cells, while T cells from the blood of individuals with brain cancer or HDs clustered together (Fig. 2a, top, and Supplementary Table 2a). $CD4^+$ and $CD8^+$ T cell populations separated within both the blood and the tumor samples (Fig. 2a, bottom). Using the Molecular Signatures Database (MSigDB) C7 collection of immunologic signature gene sets, gene set enrichment analysis (GSEA) between blood T cells and TILs revealed $CD4^+$ and $CD8^+$ activation and differentiation gene sets among the highest enriched in TILs, while gene sets of naive T cells were enriched in the matched blood samples (Fig. 2b, Extended Data Fig. 2b and Supplementary Table 2b). To confirm these findings, we evaluated the expression of different CD45 isoforms by using FCM (Extended Data Fig. 2c). Compared to HDs and matched blood T cells, which were 40–50% $CD45RO^+$, >90% of TILs were $CD45RO^+$ (Fig. 2c). Taken together, these data indicate a conserved broad activation and differentiation program in brain TILs that appears to be independent of the underlying disease.

We next investigated the extent of inter-individual heterogeneity, particularly to uncover potential differences between glioma and BrM TILs when examined at higher granularity. We focused on $CD8^+$ T cells (data are available for 47/54 individuals), as they can drive cytotoxic antitumor immunity and showed transcriptional differences between glioma and BrM in the scRNA-seq analysis (Fig. 1e). DEA between TILs and matched blood $CD8^+$ T cells revealed 997 differentially expressed genes (DEGs) detected in BrM and 670 in glioma, of which, 476 were shared between both groups (Fig. 2d, Extended Data Fig. 2d and Supplementary Table 2c). Broad T cell activation markers, including *FOSB*, *DUSP4* and *HSPA1B*, were among the top shared DEGs expressed at higher levels in TILs (Fig. 2d). By contrast, genes indicative of a naive T cell state, such as *SELL*, *TCF7* and *LEF1*, were expressed at higher levels in circulating $CD8^+$ T cells, thereby confirming the GSEA results (Fig. 2b,d). Direct comparison of BrM $CD8^+$ TILs with glioma $CD8^+$ TILs revealed *CXCL13* as the most highly DEG (Fig. 2d and Extended Data Fig. 2e). Of note, the expression of *CXCL13* in BrM TILs showed substantial inter-individual heterogeneity (Extended Data Fig. 2f).

As *CXCL13* was also the most enriched gene in the scRNA-seq pTRT cell cluster C3, we next analyzed $CD8^+$ TILs for expression of the most significantly enriched genes in C3 (fold change > 1; Supplementary Table 1b). Hierarchical clustering separated the bulk RNA-seq cohort with brain cancer into two major groups: (1) mostly lung–BrM samples showing high expression of C3-specific genes and (2) gliomas and all other BrM samples with relatively low expression (Fig. 2e). Importantly, this separation of samples was independent of individual age ($P = 0.51$, Welch's t-test), prior therapy ($P = 0.75$, Fisher's exact test) or dexamethasone treatment ($P > 0.99$, Fisher's exact test; Extended Data Fig. 2g). We hypothesized that tumors with elevated expression of C3-specific genes were infiltrated with a relatively high proportion of tumor-reactive $CD8^+$ T cells and thus labeled them as pTRT cell-high BrM (Fig. 2e). The other BrM samples and all gliomas were designated pTRT cell-low, and we maintained this distinction throughout the study. In line with this reasoning, $CD8^+$ TILs from pTRT cell-high BrM showed a significantly higher enrichment of multiple neoantigen-reactive $CD8^+$ T cell gene signatures than pTRT cell-low BrM or glioma (Fig. 2f). By contrast, no enrichment of these gene signatures was observed in circulating $CD8^+$ T cells from the three subgroups (Extended Data Fig. 2h).

Abundant and clonally expanded $CD8^+$ T cells in pTRT cell-high BrM

To validate the transcriptome-based findings with an independent method and an independent cohort, we next analyzed 25 brain tumor samples by FCM (3/25 were also profiled by RNA-seq). We used CD39 as a marker of putative tumor-reactive $CD8^+$ T cells, as recently proposed in different types of cancer including non-small cell lung cancer (NSCLC), head and neck squamous cell carcinoma, colorectal cancer and melanoma[31,33,35,36] (Fig. 3a). Cells were further gated as $CCR7^{low}$ to eliminate potential contamination by bystander naive

Fig. 3 | $CD8^+$ T cells in pTRT cell-high tumors are highly abundant and clonally expanded. a, Representative FCM plot showing the gating strategy for $CD39^+CCR7^{low}CD8^+$ and $CD39^-CCR7^{low}CD8^+$ T cells. **b**, Box plot showing the percentage of $CD39^+CCR7^{low}$ cells among $CD8^+$ T cells in individuals with glioma ($n = 14$ blood and $n = 12$ tumor samples) and BrM ($n = 13$ blood and $n = 13$ tumor samples). Significance was determined with a two-sided Wilcoxon test and Benjamini–Hochberg multiple comparison correction. **c**, FCM histograms showing the expression of indicated markers in one representative pTRT cell-high sample from an individual with BrM. **d**, Box plots comparing the median fluorescence intensity of each of the markers indicated in $CD39^+CCR7^{low}CD8^+$ and $CD39^-CCR7^{low}CD8^+$ T cells in $n = 6$ individuals with pTRT cell-high BrM. Significance was determined with a paired two-sided Wilcoxon test. **e**, Box plots showing the abundance of $CD8^+$ T cells in tumors (left, $n = 14$ glioma, $n = 20$ pTRT cell-low and $n = 13$ pTRT cell-high BrM samples) and blood (right, $n = 9$ glioma, $n = 15$ pTRT cell-low and $n = 10$ pTRT cell-high BrM samples) as the proportion of all $CD45^+$ immune cells. Significance was determined by unpaired two-sided Wilcoxon test with a Benjamini–Hochberg multiple comparison correction. **f**, Box plots summarizing the diversity of TCR β-chain in tumors (left, $n = 13$ glioma, $n = 17$ pTRT cell-low and $n = 13$ pTRT cell-high BrM samples) and blood (right, $n = 9$ glioma, $n = 15$ pTRT cell-low and $n = 11$ pTRT cell-high BrM samples) as the Chao 1 index. Significance was determined by unpaired two-sided Wilcoxon test with a Benjamini–Hochberg multiple comparison correction. **g**, Scatter plots of TCR clones are shown for three representative individuals with normalized frequency of clones in the tumor and blood. Dots are colored by expansion profile (not expanded, expanded only in tumor, expanded only in blood or dually expanded) and sized by the number of clones with the same expansion statistic. **h**, Box plot summarizing the proportion of clones detected only in the tumor from the 15 most-expanded clones in $n = 11$ individuals with glioma, $n = 17$ individuals with pTRT cell-low BrM and $n = 12$ individuals with pTRT cell-high BrM. Significance was determined by unpaired two-sided Wilcoxon test with a Benjamini–Hochberg multiple comparison correction. **i**, Representative FCM plots showing Ki67 staining gated on $CD8^+$ T cells. **j**, Box plots showing the percentage of $Ki67^+$ cells among $CD8^+$ T cells in $n = 12$ glioma, $n = 7$ pTRT cell-low BrM and $n = 6$ pTRT cell-high BrM tumor samples, and $n = 14$ glioma, $n = 8$ pTRT cell-low BrM and $n = 5$ pTRT cell-high BrM blood samples. Significance was determined by unpaired two-sided Wilcoxon test with a Benjamini–Hochberg multiple comparison correction. **k**, Stacked bar plots showing the mean proportion of $Ki67^+CD8^+$ T cells in $n = 12$ glioma, $n = 7$ pTRT cell-low BrM and $n = 6$ pTRT cell-high BrM tumor samples, and $n = 14$ glioma, $n = 8$ pTRT cell-low BrM and $n = 5$ pTRT cell-high BrM blood samples. CD39 positivity is indicated in green. Box plots in **b**, **d**–**f**, **h** and **j** are defined as explained in Fig. 2c.

https://doi.org/10.1038/s43018-023-00566-3

and memory cells[34]. $CD8^+CD39^+CCR7^{low}$ cells were almost undetectable in the blood of individuals with BrM and glioma, while among TILs, we found a significantly higher proportion in BrM than in glioma (Fig. 3b). Similar to the transcriptome analysis, this difference was driven by a subgroup of individuals with BrM (6/13) with high abundance of $CD39^+CCR7^{low}$ TILs (>30% of all $CD8^+$ T cells). We observed a significant correlation ($R^2 = 0.9285$, $P < 0.002$) between the proportion of $CD39^+CCR7^{low}$ TILs detected by FCM and the abundance of C3 in the scRNA-seq data (Extended Data Fig. 3a). Within individual samples showing high accumulation of $CD39^+CCR7^{low}$ TILs, we compared the expression of four molecules related to neoantigen-reactive T cells on $CD39^+CCR7^{low}$ versus $CD39^-CCR7^{low}$ cells (Fig. 3c). $CD39^+CCR7^{low}$ cells expressed CD103 (encoded by *ITGAE*), CXCL13, PD1 (encoded by *PDCD1*) and TIM3 (encoded by *HAVCR2*) at significantly higher levels than their $CD39^-$ counterparts, indicating that the $CD39^+CCR7^{low}$ population indeed contains pTRT cells (Fig. 3d).

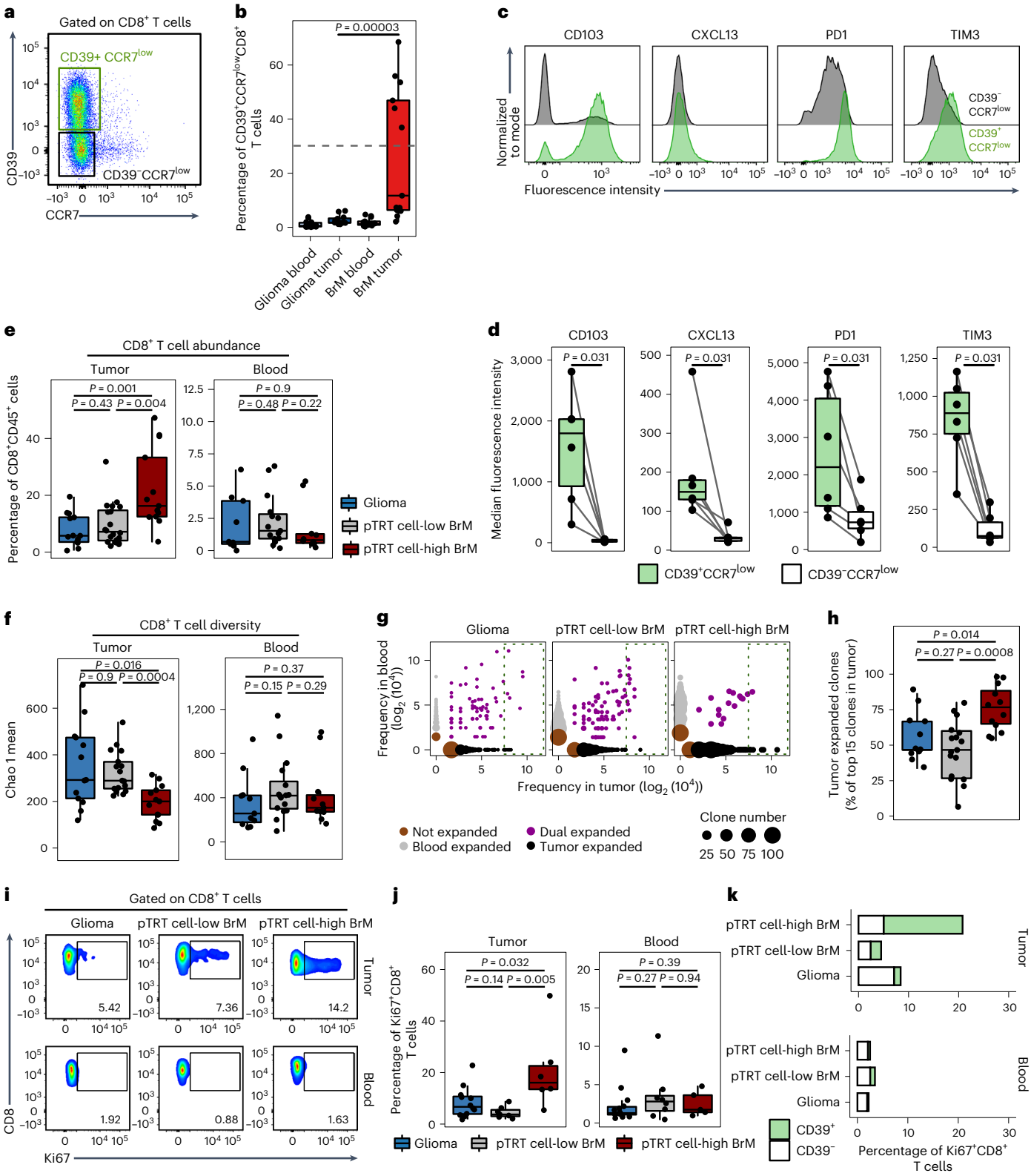

https://doi.org/10.1038/s43018-023-00566-3

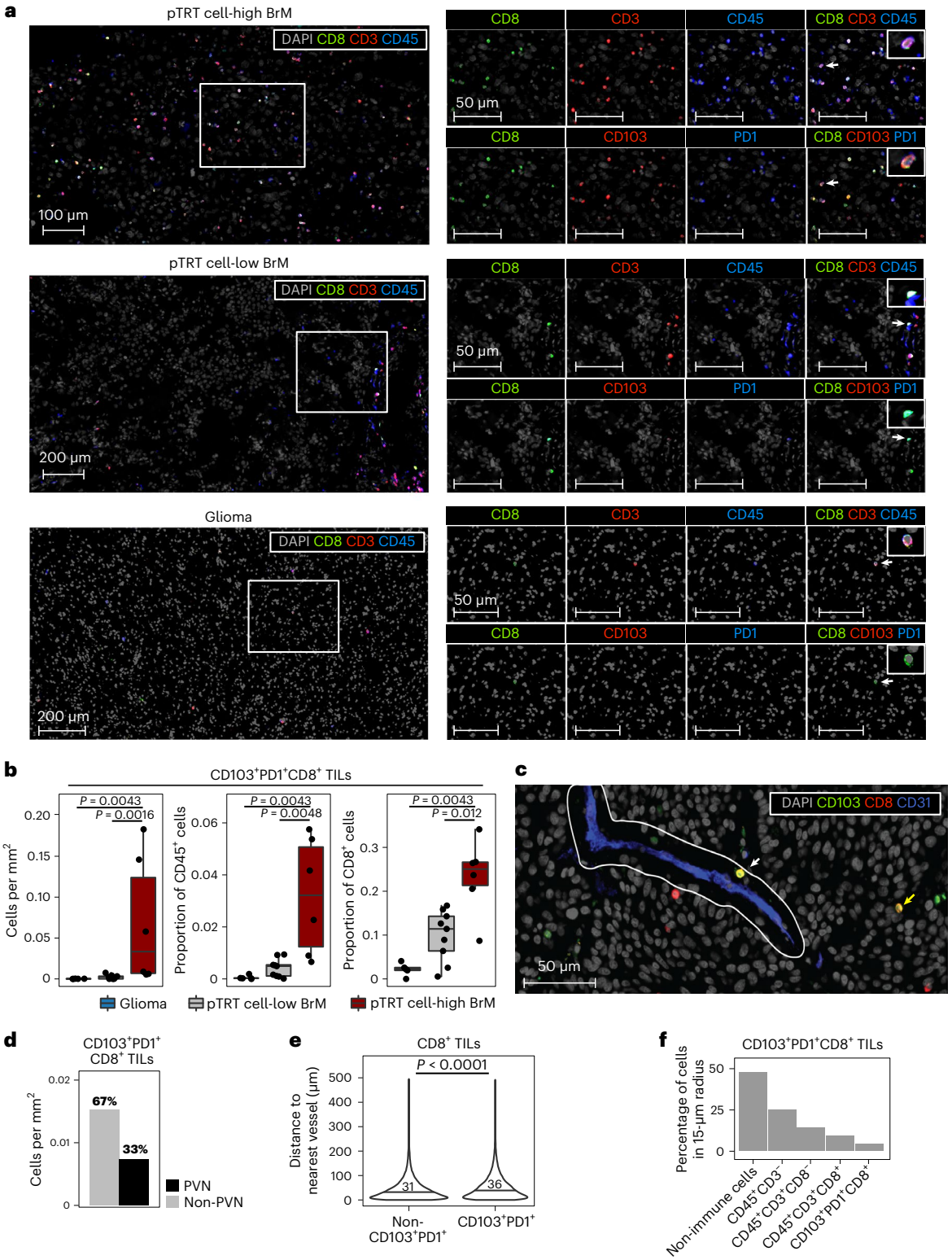

Fig. 4 | pTRT cells in BrM are located in PVNs and the stroma and within tumor nests. a, Representative IF images from a pTRT cell-high BrM, a pTRT cell-low BrM and a glioma. Insets on the far right of each image show a higher magnification of the CD8$^+$ T cell indicated by a white arrow. **b**, Box plots showing the quantification of CD103$^+$PD1$^+$CD8$^+$ TILs in $n = 5$ glioma, $n = 9$ pTRT cell-low BrM and $n = 6$ pTRT cell-high BrM tumor samples, shown as cells per square millimeter (left), proportion of CD45$^+$ cells (middle) and proportion of CD8$^+$ cells (right). Significance was determined by unpaired two-sided Wilcoxon test with a Benjamini–Hochberg multiple comparison correction. Box plots are defined as explained in Fig. 2c. **c**, Representative image of T cells within (white arrow) and outside (yellow arrow) the PVN, defined as a 15-µm radius surrounding the nearest vessel. **d**, Quantification of CD103$^+$PD1$^+$CD8$^+$ TILs within or outside the PVN ($n = 79{,}586$ CD8$^+$ T cells). **e**, Violin plot showing the mean distance of CD8$^+$ TILs from the respective nearest vessel stratified by the coexpression of CD103 and PD1. The mean distance for each group is indicated. Significance was determined by unpaired two-sided Wilcoxon test. **f**, Neighborhood analysis summarizing the cell types within a 20-µm radius around CD103$^+$PD1$^+$CD8$^+$ TILs.

RNA-seq and FCM analyses independently demonstrated heterogeneous abundance of potentially tumor-specific CD8$^+$ T cells in brain tumors, enabling the separation of the cohorts into three groups: glioma (pTRT cell-low), pTRT cell-low BrM and pTRT cell-high BrM. Comparison of these groups revealed substantially higher proportions of total CD8$^+$ TILs among all tumor-infiltrating immune cells in pTRT cell-high BrM than in pTRT cell-low BrM or gliomas (Fig. 3e, left). No significant differences in CD8$^+$ T cell proportions were observed in the blood (Fig. 3e, right). Therefore, we investigated whether the increased proportion of CD8$^+$ TILs could be a consequence of clonal expansion and analyzed the diversity of the TCR β-chain. We found that CD8$^+$ TILs, but not circulating cells, from pTRT cell-high BrM had a significantly lower TCR diversity than pTRT cell-low BrM or gliomas, thus suggesting a larger clonal expansion in these samples (Fig. 3f). Furthermore, a substantial proportion of highly expanded TCRs in pTRT cell-high BrM were not detected in matched blood samples, potentially indicating tumor-specific expansion (Fig. 3g,h and Extended Data Fig. 3b). By contrast, expanded TCRs in pTRT cell-low BrM and gliomas were also frequently present in the blood, suggesting a cancer-unrelated specificity, such as against viral antigens (Fig. 3g,h and Extended Data Fig. 3). Moreover, FCM analysis revealed more Ki67$^+$CD8$^+$ T cells in pTRT cell-high BrM than in other brain tumors (Fig. 3i,j). Of note, the majority of Ki67$^+$ cells in pTRT cell-high BrM were CD39$^+$ (Fig. 3k). Together, these findings further support the hypothesis that pTRT cell-high BrM harbor a relatively high proportion of clonally expanded tumor antigen-specific CD8$^+$ T cells.

pTRT cells are found in BrM perivascular niches (PVNs), stroma and tumor nests

We next queried the spatial organization of T cells, and especially pTRT cells, in brain tumors. We performed multiplexed IF staining of tissue sections from 20 individuals with brain cancer (Extended Data Fig. 4a). Because CXCL13 (secreted protein) and CD39 (expressed at higher levels on vessels than on T cells) were not suitable for IF, we used the coexpression of CD103 and PD1 on CD45$^+$CD3$^+$CD8$^+$ T cells as a readout for potential tumor specificity (Extended Data Fig. 4b). Individuals with BrM were stratified into pTRT cell-high or pTRT cell-low, respectively, based on the frequency of C3 determined by scRNA-seq, the enrichment of C3-specific genes in CD8$^+$ T cells analyzed by bulk RNA-seq or the abundance of CD39$^+$CCR7^{low}CD8$^+$ T cells detected by FCM (Extended Data Fig. 4c). Group assignment by the different methods was identical in those samples analyzed by more than one technology (Extended Data Fig. 4d). CD103$^+$PD1$^+$CD8$^+$ TILs were substantially more abundant in pTRT cell-high BrM than in pTRT cell-low BrM or gliomas (Fig. 4a,b). Moreover, we observed higher total CD8$^+$ TIL infiltration in pTRT cell-high BrM by IF (Extended Data Fig. 4e), recapitulating the FCM analysis in Fig. 3e.

Because blood vessels are the main entry site for T cells into brain tumors, we next studied the spatial relationship between the vasculature and CD103$^+$PD1$^+$CD8$^+$ TILs. We defined the PVN as a region surrounding CD31$^+$ vessels with a diameter of 15 µm and found that one-third of CD103$^+$PD1$^+$CD8$^+$ TILs were located within the PVN (Fig. 4c,d and Extended Data Fig. 4f,g). Two-thirds of pTRT cells were located outside the PVN and were infiltrating the brain tumor tissue (Fig. 4d and Extended Data Fig. 4f,g). CD103$^+$PD1$^+$CD8$^+$ TILs were significantly further away from the nearest vessel than all other CD8$^+$ TIL populations (denoted 'non-CD103$^+$PD1$^+$'), indicating deeper penetration into the tissue (Fig. 4e). Neighborhood analysis showed that the majority of CD103$^+$PD1$^+$CD8$^+$ TILs were in close proximity to non-immune cells (Fig. 4f and Extended Data Fig. 4h,i). A separate analysis of the same tissues revealed that, on average, 80% of CD45$^-$ non-immune cells in BrM were pan-cadherin$^+$ tumor cells, indicating that pTRT cells are present within tumor nests (Fig. 4f and Extended Data Fig. 4j).

Finally, we combined the results from the single-cell methods (scRNA-seq, FCM and IF) to validate the observations generated by bulk RNA-seq of sorted CD8$^+$ T cells (Fig. 2). We found a significant positive correlation between the true abundance of pTRT cells among all CD8$^+$ T cells (measured by scRNA-seq, FCM and IF) and the computationally imputed pTRT cell frequencies in bulk RNA-seq data using C3-specific genes (Extended Data Fig. 4k), confirming the validity of this approach.

A distinct myeloid cell subtype is associated with high pTRT cell abundance

We next investigated whether high pTRT cell abundance was associated with a distinct tumor microenvironment, particularly with respect to myeloid cells, which have been shown to regulate the function of tumor-specific T cells in kidney, prostate, bladder and ovarian cancer[37,38]. Spatial imaging analysis of >4 × 10^6 cells across 25 samples revealed that in pTRT cell-high BrM, a larger proportion of CD8$^+$ TILs was in close proximity (20 µm) to tumor-associated macrophages (TAMs), which include resident microglia (MG; identified as CD45$^+$CD68$^+$ and/or P2RY12$^+$CD49D$^-$) and recruited monocyte-derived macrophages (MDMs; identified as CD45$^+$CD68$^+$ and/or P2RY12$^+$CD49D$^+$), compared to glioma or pTRT cell-low BrM (Fig. 5a), allowing for potential direct cellular interactions. This observation could be partially influenced by the higher proportion of total CD8$^+$ TILs in pTRT cell-high BrM (Extended Data Fig. 4e). Thus, we next analyzed the distance between CD8$^+$ TILs and their respective nearest TAMs. We found that CD103$^+$PD1$^+$CD8$^+$ TILs

Fig. 5 | Myeloid cells with antigen presentation capacity are associated with high pTRT cell abundance. a, Box plots showing the percentage of CD8$^+$ TILs within a 20-µm radius around MG (top) or MDMs (bottom) in $n = 6$ individuals with glioma, $n = 12$ individuals with pTRT cell-low BrM and $n = 7$ individuals with pTRT cell-high BrM. Significance was determined by unpaired two-sided Wilcoxon test with a Benjamini–Hochberg multiple comparison correction. **b**, Violin plots showing the distance of CD8$^+$ TILs from the respective nearest TAM (MG, top; MDMs, bottom) stratified by the coexpression of CD103 and PD1 in $n = 5$ individuals with glioma and $n = 16$ individuals with BrM. The mean distance for each group is indicated. Significance was determined by unpaired two-sided Wilcoxon test. **c**, Balloon plot showing results from a GSEA of Hallmark and Gene Ontology biological process gene sets in MDMs and MG from pTRT cell-high BrM versus pTRT cell-low BrM or gliomas, respectively. Pathways mentioned in the main text are highlighted in black. Adjusted *P* values (Benjamini–Hochberg method) and normalized enrichment scores (NES) were calculated with the fgsea package in R; IL-6, interleukin 6; P_{adj}, adjusted *P* value. **d**, Dot plots indicating a correlation between the expression of antigen presentation programs in MG (top) or MDMs (bottom) and the pTRT cell signature enrichment in CD8$^+$ T cells. Significance was determined by linear regression. Dots are colored by disease group; $n = 13$ individuals with glioma, $n_{MG} = 17$ individuals with pTRT cell-low BrM, $n_{MDM} = 20$ individuals with pTRT cell-low BrM and $n = 12$ individuals with pTRT cell-high BrM. **e**, Box plots showing the expression of T cell recruitment cytokines as $\log_2$ (CPM) in $n = 13$ individuals with glioma, $n_{MG} = 17$ individuals with pTRT cell-low BrM, $n_{MDM} = 20$ individuals with pTRT cell-low BrM and $n = 12$ individuals with pTRT cell-high BrM. Adjusted *P* values (Benjamini–Hochberg method) were calculated with the limma package in R. CPM, counts per million. **f**, Dot plots indicating the correlation between the abundance of CD8$^+$ T cells and the expression of *CXCL9*, *CXCL10* and *CXCL11* in MG (left) or MDMs (right). Significance was determined by linear regression. Dots are colored by disease group; $n = 13$ individuals with glioma, $n_{MG} = 17$ individuals with pTRT cell-low BrM, $n_{MDM} = 20$ individuals with pTRT cell-low BrM and $n = 12$ individuals with pTRT cell-high BrM. **g**, Schematic of the ex vivo anti-PD1 treatment and T cell proliferation assay. **h**, Summary of ex vivo T cell proliferation in $n = 7$ glioma (left) and $n = 10$ BrM (right) tumor samples under the indicated conditions. Samples showing a proliferation increase compared to both untreated (Untr) and isotype control (Iso) conditions are highlighted; aPD1, anti-PD1. **i**, Pie charts indicating the disease group of $n = 7$ glioma and $n = 8$ BrM tumors used in the ex vivo proliferation assay profiled by at least one other method (FCM or RNA-seq) and grouped by their response to anti-PD1. Box plots in Fig. 5a,e are defined as explained in Fig. 2c.

https://doi.org/10.1038/s43018-023-00566-3

were located significantly, albeit modestly, closer to the nearest MG and had the same distance to the nearest MDM as all other CD8$^+$ TILs (Fig. 5b and Extended Data Fig. 5). These results indicate a similar likelihood for pTRT cells and non-pTRT cells to communicate with TAMs.

We next examined whether there was a difference in the potential for TAM–T cell communication specifically when comparing the pTRT cell-high and cell-low tumors identified herein. We analyzed the transcriptomes of sorted MG and MDMs from the same tumor

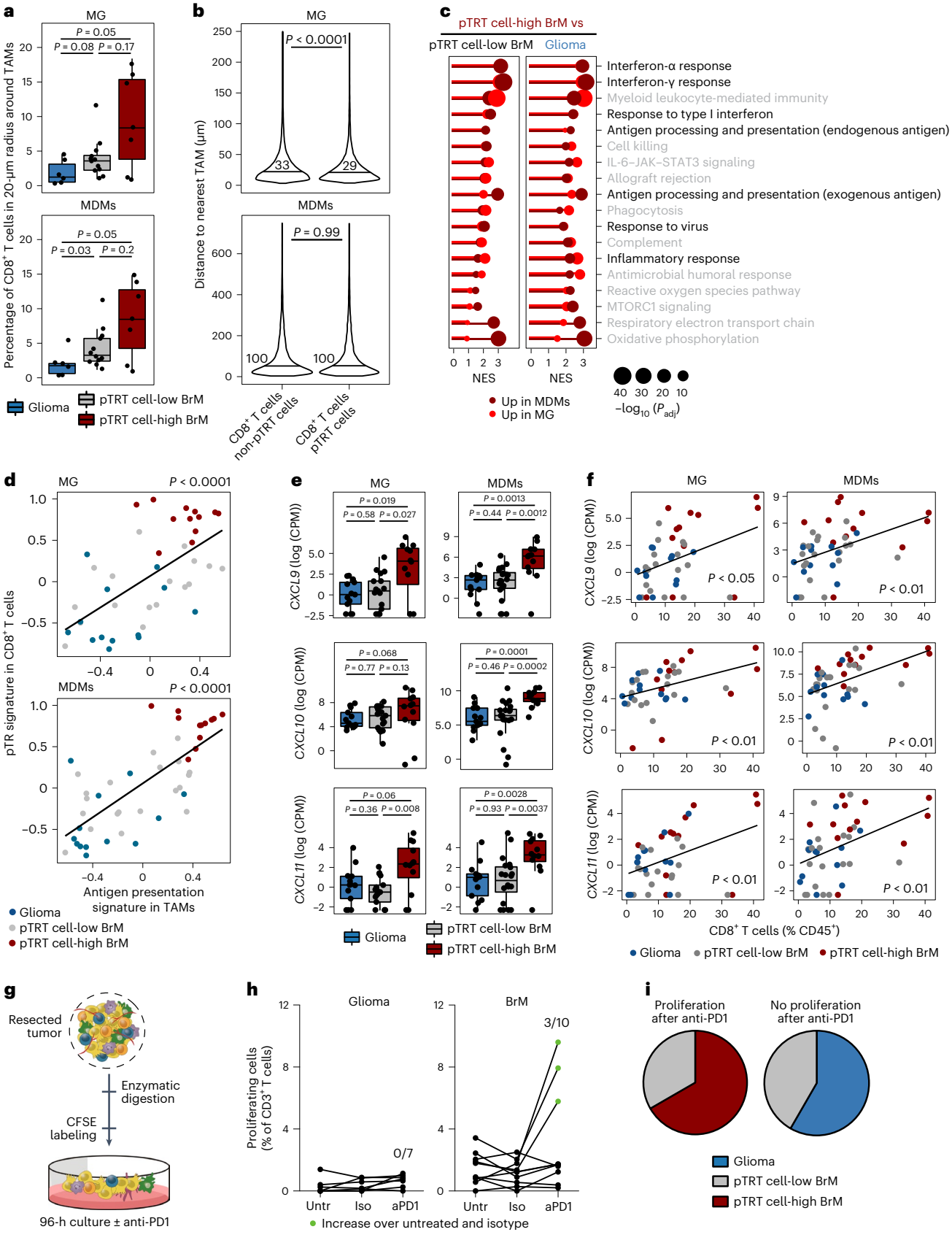

samples from which we had also collected T cells (Extended Data Fig. 6a,b). GSEA using Hallmark and Gene Ontology biological process gene sets revealed substantial differences in both MG and MDMs (Fig. 5c and Supplementary Table 3a). In particular, gene sets associated with interferon response and antigen presentation were highly enriched in TAM populations isolated from pTRT cell-high BrM compared to those in pTRT cell-low BrM and glioma samples (Fig. 5c). Moreover, there was a robust correlation between the enrichment of antigen presentation genes in TAMs and the enrichment of pTRT cell signature genes in $CD8^+$ T cells (Fig. 5d). DEA confirmed the elevation of interferon response and antigen presentation genes and also revealed significantly higher expression of the T cell recruitment molecules *CXCL9*, *CXCL10* and *CXCL11* in TAMs from pTRT cell-high BrM (Fig. 5e, Extended Data Fig. 6b and Supplementary Table 3b). Furthermore, the expression level of T cell-recruiting chemokines in TAMs correlated significantly with the abundance of $CD8^+$ T cells in the same samples (Fig. 5f). Of note, in addition to the ability to recruit and activate T cells, TAMs from pTRT cell-high BrM expressed high levels of *IDO1*, suggesting that they may also possess T cell-suppressive properties (Extended Data Fig. 6c).

Myeloid antigen-presenting cell niches have also been shown to regulate anti-PD1 efficacy[37], and *CXCL9* expression in the tumor microenvironment can predict response to ICB therapy[23]. We therefore next evaluated whether brain TIL proliferation could be stimulated with anti-PD1 treatment ex vivo. We used a previously established 96-h experimental assay[37] and measured carboxyfluorescein succinimidyl ester (CFSE) dilution specifically in T cells by FCM (Fig. 5g). It is important to note that we were unable to incorporate cognate tumor antigen peptides in this experimental design due to the current lack of validated common targets in primary and metastatic brain cancers. Nonetheless, using this strategy, we found that T cell proliferation could not be increased ex vivo via anti-PD1 treatment in glioma samples (zero of seven), while in BrM, we observed a proliferation increase following anti-PD1 treatment in three of ten samples (Fig. 5h and Extended Data Fig. 6d). By contrast, nonspecific activation with anti-CD3/anti-CD28 induced proliferation in glioma and BrM TILs to a similar extent, suggesting that functional T cells can be found in both pathologies (Extended Data Fig. 6e,f). Fifteen of the 17 tumors analyzed for proliferation following anti-PD1 treatment in this assay were also profiled by bulk RNA-seq, FCM or IF and thus contained information regarding pTRT cell status. Two of three proliferating samples were pTRT cell-high BrM, while non-proliferating samples contained only pTRT cell-low BrM and gliomas (Fig. 5i). Thus, interferon-stimulated TAMs with antigen-presenting and T cell-recruiting capacities in certain BrM lesions may represent an important mechanism that enables the high abundance of pTRT cells in vivo and that may potentially influence the response to anti-PD1 treatment.

Comparison of pTRT cells in BrM versus extracranial cancer

While little is currently known about pTRT cells in brain cancers, these cells have been investigated in several extracranial tumor types[26]. Therefore, we next compared pTRT cells in intracranial and extracranial tumors. We began by analyzing scRNA-seq data from 21 different extracranial cancer types and 316 individuals[26] for the expression of the top ten genes in BrM pTRT cell scRNA-seq cluster C3. Interestingly, we found the highest expression of all ten genes within the CD8.c12.Tex.CXCL13 cluster, which has been annotated to contain the largest proportion of pTRT cells, thereby indicating similarities between intracranial and extracranial pTRT cells (Fig. 6a).

To further extend these findings, we performed high-dimensional FCM analyses on an additional cohort of TILs and blood T cells isolated from 12 individuals with glioma (8 *IDH* wild type and 4 *IDH* mutant), 13 individuals with BrM (10 NSCLC, 1 melanoma, 1 epidermoid cancer and 1 sarcoma), 11 individuals with primary BC and 33 individuals with NSCLC (Fig. 6b and Supplementary Tables 1a and 4). As above, we focused on $CD8^+$ T cells. Following normalization of these data, we performed unsupervised clustering and defined 12 distinct cytometry clusters (CCs), several of which showed a clear tissue-specific prevalence (Fig. 6c and Extended Data Fig. 7a,b). Analysis of individual proteins allowed us to identify one pTRT cell cluster, CC9, expressing high levels of CD39, CXCL13, TIM3, PD1 and CD45RO (Fig. 6d). As expected, blood samples from all disease groups lacked cells of CC9, while in tumors, these cells were detected at varying frequencies (Fig. 6d,e and Extended Data Fig. 7a). In gliomas and primary BC tumors, CC9 cells comprised, on average, 5% of all $CD8^+$ TILs, with only 1 BC tumor sample (1/11) displaying high CC9 abundance (Fig. 6e,f). By contrast, the vast majority of primary NSCLC tumors showed a high infiltration of CC9 cells, representing 25% of TILs on average. In BrM, we could again discriminate two groups of individuals, one with low CC9 (7/13) and one with high CC9 (6/13) abundance (Fig. 6f). The six BrM tumors with high CC9 abundance included one of one melanoma–BrM and five of ten NSCLC–BrM. Of note, in primary NSCLC and BrM tumors with a high proportion of CC9 (>30%), the abundance of these cells was similar (Fig. 6e,f). In general, CC9 was among the most variable across the disease groups (Extended Data Fig. 7c).

We independently confirmed these findings by manually gating for $CD39^{high}CCR7^{low}CD8^+$ T cells and obtained very similar results (Fig. 6g,h). Finally, we compared the phenotype of $CD39^{high}CCR7^{low}CD8^+$ TILs (pTRT cells) between the different tumor types. As only two of the glioma tumors had >100 pTRT cells, we excluded glioma samples from this specific analysis. We found several molecules enriched in primary NSCLC pTRT cells compared to BC and BrM pTRT cells, including ICOS, TIM3, CXCL13 and CD103 (Fig. 6i). By contrast, CD38, HLA-DR, GZMB and PD1 were highly expressed in BrM pTRT cells compared to pTRT cells in primary BC and NSCLC (Fig. 6i). Together, these analyses revealed that while the pTRT cell abundance was similar in primary NSCLC and BrM, particularly melanoma–BrM and NSCLC–BrM, the pTRT cell phenotype showed some underlying disease specificity.

Discussion

In this study, we applied a diverse panel of orthogonal analyses to systematically and comprehensively profile T cells in primary and metastatic brain cancers. Our analysis revealed both phenotypic similarities

Fig. 6 | Abundance of pTRT cells in BrM and primary NSCLC is comparable, while the phenotypes are distinct. a, Expression heat map of the top ten genes from BrM C3 in the pan-cancer single-cell T cell atlas data. Rows represent normalized and scaled expression. Metacluster and pTRT cell status are annotated per column. **b**, Schematic of the high-dimensional FCM analysis. **c**, UMAP of the full cohort grouped by tissue with the cytometry cluster (CC) annotated. **d**, Heat map showing median scaled expression of individual markers in each cluster and the proportion among blood or tumor $CD8^+$ T cells. **e**, Box plot visualizing the abundance of the pTRT cell cluster CC9 in $n = 11$ individuals with BC, $n = 32$ individuals with NSCLC, $n = 12$ individuals with glioma and $n = 12$ individuals with BrM. Significance was determined with a Kruskal–Wallis test and a Benjamini–Hochberg multiple comparison correction. **f**, Stacked bar plots showing the abundance of each cluster in individual tumors grouped by disease. **g**, Representative FCM plots illustrating the expression of CD39 and CCR7 in the blood and tumor of each disease group. **h**, Box plot summarizing the abundance of $CD39^+CCR7^{low}$ cells among all $CD8^+$ T cells in the blood of $n = 11$ individuals with BC, $n = 33$ individuals with NSCLC, $n = 14$ individuals with glioma and $n = 13$ individuals with BrM, and in the tumors of $n = 11$ individuals with BC, $n = 32$ individuals with NSCLC, $n = 12$ individuals with glioma and $n = 13$ individuals with BrM. Significance was determined with a Kruskal–Wallis test with a Benjamini–Hochberg multiple comparison correction. **i**, Box plots showing median fluorescence intensity of the indicated markers expressed on $CD39^+CCR7^{low}CD8^+$ TILs from $n = 8$ individuals with BC, $n = 29$ individuals with NSCLC and $n = 9$ individuals with BrM. Significance was determined by a Kruskal–Wallis test with a Benjamini–Hochberg multiple comparison correction. Box plots in Fig. 6e,h,i are defined as explained in Fig. 2c.

https://doi.org/10.1038/s43018-023-00566-3

and differences when interrogating TILs from BrM and glioma. The similarities were largely driven by T cell activation and differentiation, indicating the requirement of these processes for T cells to infiltrate brain tumor tissue. Similar observations have been made in several extracranial cancer types[26,39]. Importantly, our results indicate that in the majority of individuals with primary and metastatic brain cancer analyzed herein, activated TILs were likely not reactive against the tumor and were generally low in abundance. These pTRT cell-low

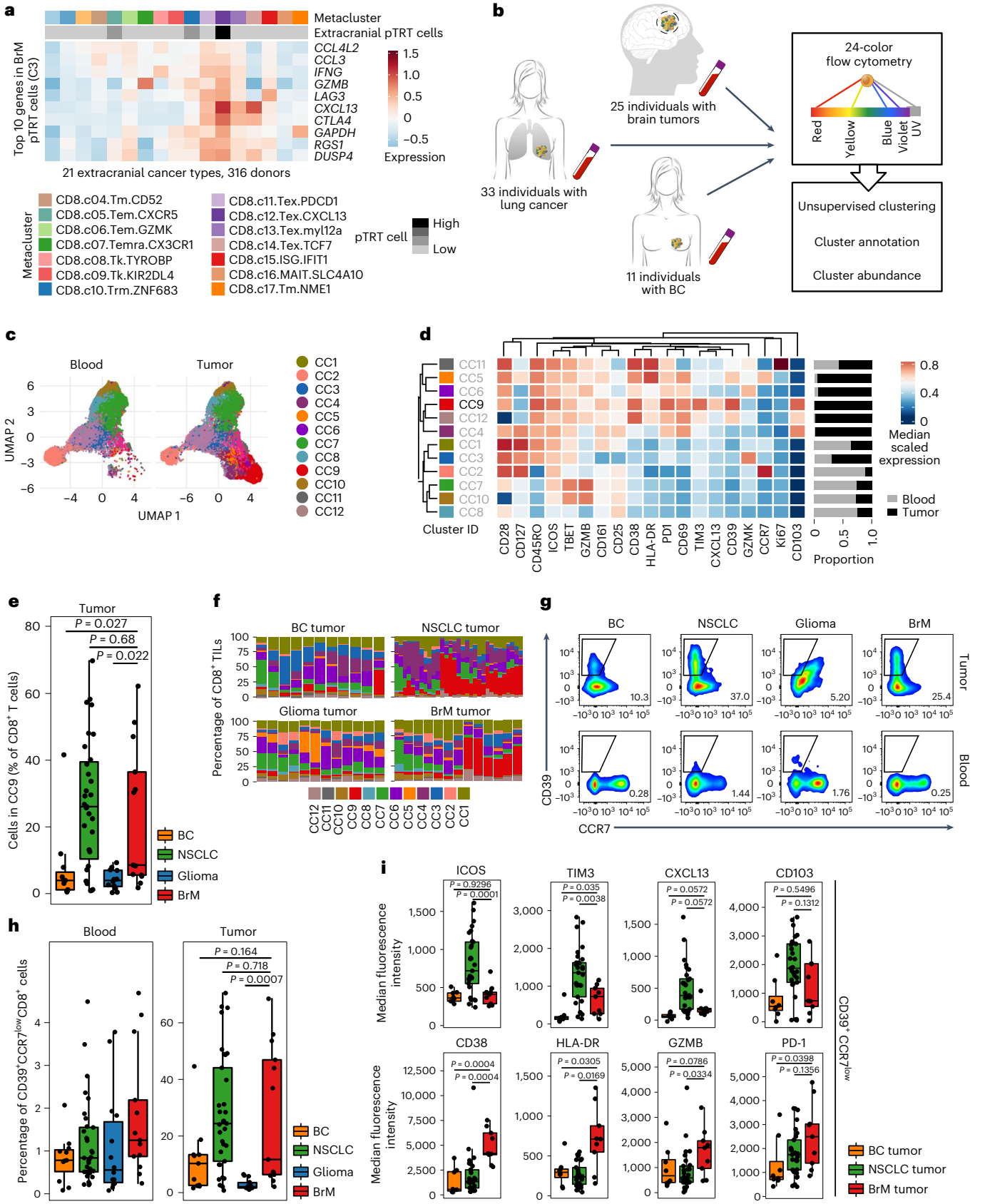

tumors additionally showed signs of a non-inflamed 'cold' tumor microenvironment[40] with relatively low levels of inflammatory and T cell-recruiting cytokines. Among potential mechanisms facilitating this environment are the physical exclusion of T cells from tumor nests through an aberrant vasculature, the engagement of different chemokine signaling pathways, including transforming growth factor-β (TGFβ) and CXCL12 (refs. 41–44), or an insufficient availability of tumor-specific/tumor-associated antigens[45]. Indeed, we found enrichment for TGFβ response genes in MDMs from pTRT cell-low BrM and glioma compared to in pTRT cell-high tumors (data not shown). Additionally, the majority of tumors classified as pTRT cell-low herein were either glioma or breast–BrM, and both are characterized by a relatively low somatic mutation prevalence[46].

However, we identified a subset of individuals with BrM with a distinct $CD8^+$ TIL phenotype, characterized by high *CXCL13* RNA expression, high CD39 protein levels and the enrichment of a dysfunctional gene signature. $CD8^+$ TILs in these pTRT cell-high BrM were clonally expanded, showed little clonal overlap with matched blood $CD8^+$ T cells and were located predominantly within tumor nests, suggesting specific tumor reactivity[16,35]. FCM and scRNA-seq analyses confirmed the presence of a $CD8^+$ T cell population with a tumor reactivity phenotype in pTRT cell-high BrM, accounting for at least 30% of all $CD8^+$ T cells. Approximately 50% of all analyzed BrM samples, and none of the gliomas, displayed such a pTRT cell-high tumor microenvironment. The infiltration of BrM tumors with pTRT cells has recently been reported[47], however, without exploring the inter-individual heterogeneity. Here, we show that pTRT cell abundance differs substantially between primary and metastatic brain cancers and between individuals with BrM, even with the same disease subtype.

These findings naturally raise the question as to why the disease progresses in pTRT cell-high BrM. Several mechanisms that can suppress pTRT cell function have been described in other cancers[41], including the accumulation of inhibitory cells in the tumor microenvironment, such as T_{reg} cells[48] and suppressive myeloid cells[49], as well as the release of soluble immunosuppressive molecules (for example, IDO1)[50]. These mechanisms could also play a role in pTRT cell-high BrM. Indeed, we found that T_{reg} cells were more prevalent in BrM than in gliomas, both in this study and in a recent analysis of the global brain immune cell landscape[5], possibly resulting from increased tumor reactivity overall. Moreover, we determined that *IDO1*, which catabolizes tryptophan into the immunosuppressive metabolite kynurenine, is expressed at significantly higher levels in MDMs and MG isolated from pTRT cell-high BrM than those from pTRT cell-low BrM or glioma. However, it is important to note that different TAM subpopulations in pTRT cell-high BrM likely have distinct roles, immunosuppressive and inflammatory. In fact, we found higher expression of multiple T cell-recruiting molecules by MDMs and MG in pTRT cell-high BrM, along with genes involved in antigen presentation. Similar complex TAM phenotypes have been shown to support pTRT cells in ovarian, kidney, prostate and bladder cancer[37,38]. As such, several distinct subpopulations of TAMs may coexist in pTRT cell-high tumors, executing either immune suppression or inflammation, and likely depend on the spatial cues they are subject to within their local tumor microenvironment niche, as recent findings would suggest[51].

In summary, this study has important implications for the clinical management of individuals with brain cancer. The abundance of *CXCL13*-expressing ($CD39^+$) $CD8^+$ T cells and the expression of *CXCL9* in the tumor microenvironment are robust predictors for ICB response in many different primary cancer types, including lung and triple-negative BC[22–24,52]. These factors may also indicate ICB susceptibility in the brain, and we found both to be significantly enriched in pTRT cell-high BrM. In addition, the proportion of $CXCL13^+CD39^+CD8^+$ TILs in pTRT cell-high BrM was similar to that in primary NSCLC, one of the most responsive cancers to ICB[53]. This suggests that only individuals with pTRT cell-high, but not pTRT cell-low, tumors would potentially benefit from this treatment. While it remains an open question regarding how to evaluate the pTRT cell status of a brain tumor without surgical resection, our data provide the rationale to intensify research into minimal and non-invasive procedures to assess the quantity and quality of T cells within brain tumors.

Methods

Study approval

All experimental procedures performed on clinical tissue samples obtained from individuals were in accordance with the ethical standards of the institutional and national research committees and with the 1964 Helsinki Declaration and its later amendments or comparable ethical standards. Informed consent was obtained from all participants included in this study. The collection of tumor and non-tumor tissue and blood samples from individuals with brain disease at the Biobank of the Brain and Spine Tumor Center (BB_031_BBLBGT) of the Centre Hospitalier Universitaire Vaudois (Lausanne, Switzerland) was approved by the Commission Cantonale d'éthique de la Recherche sur l'être Humain (CER-VD, protocol PB 2017-00240, F25/99). The use of human samples from individuals with extracranial disease was approved by the Humanitas Clinical and Research Center Institutional Review Board (Milan, Italy) under the following protocols: lung cancer tissue and blood samples from individuals with NSCLC (1501) and BC tissue and blood from individuals with BC (ONC-OSS-02-2017). Tissue specimens were immediately collected from the operating room and processed as described below. All samples were fully anonymized. All available clinical information is included in Supplementary Table 1a.

Clinical sample handling and processing

Clinical sample processing and preparation for conventional FCM, fluorescence-activated cell sorting and RNA-seq of sorted populations (bulk RNA-seq) were performed as described previously[27], module 2. For cryopreservation, 0.5×10^6–2×10^6 cells were resuspended in ice-cold freezing medium containing 90% fetal bovine serum (Gibco) and 10% DMSO (Applichem), placed at −80 °C overnight in an alcohol-free freezing container (Corning, CoolCell) and transferred thereafter to liquid nitrogen for long-term storage. Cryopreserved samples were recovered by rapid thawing at 37 °C and were subsequently washed in complete medium comprised of DMEM/F12 (Thermo Fisher Scientific, 11320033), 10% fetal bovine serum and 1% penicillin–streptomycin (Thermo Fisher Scientific, 15070063).

High-dimensional FCM

High-dimensional FCM was performed as described previously[54]. Dead cells were excluded from all analyses using Zombie Aqua (BioLegend). Fluorochrome-conjugated monoclonal antibodies were purchased from commercial vendors (Supplementary Table 5a). All reagents were titrated before use to determine optimal concentrations. Transcription factors and intranuclear molecules were measured in conjunction with a transcription factor buffer set (BD Biosciences). Samples were acquired using a FACSymphony A5 equipped with FACSDiva software version 8.0.1 (BD Biosciences). Electronic compensation was performed using single-stained controls prepared with antibody capture beads (BD Biosciences).

Bioinformatic analysis environment

All bioinformatic analyses were performed within the R environment version 4.0.3 and Bioconductor version 3.12.

Bulk RNA-seq, count matrix generation

Immune cell populations were sorted based on the markers and gating strategy described previously[5]. RNA extraction, library preparation and sequencing of sorted populations were performed at Genewiz Services (http://www.genewiz.com/) using the ultralow input RNA-seq service, which uses a poly(A) selection with enrichment for full-length

transcripts. Paired-end sequencing of the libraries was performed using an Illumina HiSeq instrument with 2 × 150-base pair configuration. Raw sequencing reads were aligned to a reference human genome using STAR v2.7.7a[55], and counts were quantified using RSEM v1.3.3 (ref. 56). Human genome version 38 was used with GENCODE v36 annotation. Raw counts of transcripts with the same gene symbol were pooled. Samples with <1,000,000 total counts were excluded.

RSEM counts of T cells were further processed to account for potential contamination with transcriptionally highly active tumor cells (sorted as $CD45^-$ cells). A four-step process was applied for each disease group: (1) selecting 250 genes with highest absolute expression in $CD45^-$ cells, (2) performing DEA between $CD45^-$ cells and all T cells (blood and tumor) using the limma (RRID SCR_010943) package[57], (3) identifying genes expressed at substantially higher levels in $CD45^-$ cells than in T cells using very stringent cutoffs with a fold change of >3 and FDR of <0.001 and (4) generating overlap between DEGs from (3) and highly expressed tumor cell-specific genes from (1). The resulting genes (a total of 136) were removed from the count matrix (Supplementary Table 5b).

Bulk RNA-seq, gene-focused analysis

All visualizations of counts are displayed as $\log_2$ (CPM) generated with the limma package. Annotated heat maps were generated with the pheatmap (RRID SCR_016418) package and show the expression of individual genes as *z* scores and are clustered using Euclidean distance. The 250 most variably expressed genes among all T cells were identified as those 250 genes with the largest variance in expression. For DEA, counts were first filtered using the filterByExpr function from the edgeR package (RRID SCR_012802)[58] and normalized using the trimmed mean of the M values method (edgeR). The limma voom function was used to perform DEA. Significance cutoffs of a fold change of >2 or <−2 and an FDR of <0.05 were used.

Bulk RNA-seq, pathway-centered analysis

Pathway enrichment in sample groups was analyzed by GSEA using the fgsea (RRID SCR_020938) package, considering pathways with a minimum size of 15 and maximum size of 500 genes. Gene ranks for fgsea were derived from the *t*-statistic of limma. Pathway enrichment in individual samples was analyzed by gene set variation analysis using the gsva method and $\log_2$ (CPM) as input. Hallmark, Gene Ontology biological process and C7 gene sets were obtained from MSigDB[59] (version 7.2.1) using the msigdbr package. The C7 gene set collection was filtered to contain only pathways with 'CD4' or 'CD8' in their title.

TCR analysis from bulk RNA-seq

To derive individual TCR β-chain sequences from our bulk RNA-seq data, the mixcr framework[60] was used with default parameters. Briefly, the raw reads were cleaned from adaptor sequences using Trimmomatic[61], and duplicated reads were removed with the clumpify function from bbmap (RRID SCR_016965). Processed reads were aligned against the reference V, D, J and C genes of the TCR (downloaded September 2019). Aligned reads were quantified, and identical reads were grouped into clonotypes. Here, only the TCR β-chain was used. The diversity of the TCR pools was evaluated with the vdj tools framework[62], and the Chao estimate was used to determine the lower bound total diversity estimates (Chao 1 index).

Sample and library preparation for single-cell sequencing

Tumor tissue and blood were prepared as for bulk RNA-seq analysis. Staining for T cell sorting was performed as for bulk RNA-seq. $CD45^+CD11B^-CD3^+CD4^+$ and $CD45^+CD11B^-CD3^+CD8^+$ cells were sorted into the same tube containing 8 µl of HBSS at 4 °C. Afterward, a maximum of 16,000 total T cells was loaded onto the 10x Chromium Controller following the manufacturer's instructions. For the generation of gel beads in emulsion (GEM), a Chromium Next GEM single cell 5′ kit v2 (10x, 1000263) and the Chromium Next GEM Chip K single cell kit (10x, 1000287) were used. Gene expression (GEX) and TCR (VDJ) libraries were prepared using the library construction kit (10x, 1000190) and Chromium single cell human TCR amplification kit (10x, 1000252), respectively, following the manufacturer's instructions.

Library quantity and quality were determined using Qubit fluorometric quantification (Thermo Fisher Scientific, Q32851) and high-sensitivity next-generation-sequencing fragment analysis (Agilent Technologies, DNF-474-0500). Sequencing was performed by Genewiz Services (http://www.genewiz.com/) on an Illumina NovaSeq6000 S4 flow cell using a 10x sequencing configuration. Targeted sequencing depth was >20,000 reads per cell for GEX and >5,000 reads per cell for VDJ libraries, respectively.

Single-cell sequencing analysis

FastQ files of the GEX and VDJ libraries were aligned to the human reference genome GRCh38 2020-A (release July 7, 2020) and to the GRCh38 _alts_ensemble-5.0.0, respectively, using Cell Ranger software (version 6.0) from 10x Genomics. Downstream analysis was performed using Seurat (RRID SCR_016341) package version 4.0 (ref. 63) in R. For visualization, Seurat, dittoSeq[64] and tidyverse (RRID SCR_019186) packages were used. For quality control, we retained only cells with <10% mitochondrial RNA and 250–3,000 total features. Samples were integrated with the SCTransform function[65] using the day of sample sorting as the batch parameter. Clustering was performed with 31 dimensions in FindNeighbors and RunUMAP functions and a resolution of 0.18 in the FindClusters function. Cluster-specific genes were identified using the FindMarkers function with a fold change of >0.25 and at least 25% of cells in each cluster expressing the DEG using the Wilcoxon rank-sum test. Results were validated by receiver operating characteristic analysis in Seurat. Neoantigen-reactive $CD8^+$ T cell gene signature scores were calculated using the AddModuleScore function. DEA between groups was performed using the FindMarkers function with the Poisson generalized linear model including batch as a covariant. VDJ libraries were processed with the scRepertoire package[66]. TCR similarity analysis was performed with the clonalOverlap function using the Morisita index.

Prediction of TCR specificity against viral antigens

VDJmatch software version 1.3.1 was used to match TCR-β repertoires (generated by scRNA-seq) against the VDJdb (https://vdjdb.cdr3.net/) database compiling curated TCR sequences with known antigen specificity. The function match was used with default parameters to align TCR sequences for each $CD8^+$ T cell cluster separately. Results were filtered using the vdjdb.score including matching sequences only with a vdjdb.score of ≥1. Unique matching viral antigens were counted and plotted.

Computational analysis of high-dimensional FCM data

FCM standard 3.0 files were imported into FlowJo software version 9 (FlowJo). A conventional gating strategy was used to remove aggregates and dead cells. Viable $CD3^+CD8^+$ T cells were exported and used for downstream analysis. FlowJo software version 10.8.1 (FlowJo) was used for all analysis requiring manual gating. For unsupervised clustering analysis, samples with <100 $CD8^+$ T cells were excluded. Remaining samples were downsampled to 1,500 cells with random sampling and imported into R using the flowCore and CATALYST packages (RRID SCR_002205). Data were transformed with arcsinh-transformation using a cofactor of 150. The flowSOM algorithm was used to cluster the cells[67]. For clustering, all markers were used with the exception of the live/dead dye, CD3, CD4, CD8 and FOXP3. Visual investigation of the different cluster numbers determined 12 as the most informative. UMAP projections were calculated with the runDR function from CATALYST.

Sequential IF staining

The optimal cutting temperature-embedded tissues (Tissue-Tek, Sakura Finetek) were cut into 10-µm-thick slices, frozen and stored at

−80 °C as outlined previously[27]. The integrity of the tissue was assessed using hematoxylin and eosin staining. Slides were air dried and fixed for 40 min at room temperature (RT) in 10% neutral buffered formalin (Fisher Scientific, Epredia 5701, 22-050-104). Afterward, the tissue was rehydrated in PBS (Gibco) by washing three times for 5 min each, followed by quenching in PBS and 10 mM glycine (Panreac Applichem ITW reagents, A1067) for 10 min at RT. The slides were then washed with PBS and 0.2% Tween (Applied Chemicals) two times for 5 min each, permeabilized with PBS and 0.2% Triton X-100 (Applied Chemicals) for 10 min and washed two times with PBS. Using an A-PAP pen, a hydrophobic circle was drawn in which the blocking solution was added for a 1-h incubation at RT inside a humidified chamber on a rocking platform. The blocking solution consisted of 1× PNB reagent (PerkinElmer, FP1012), 0.5% Tween, 10% donkey serum (Sigma-Aldrich, S30-M) and 2% bovine serum albumin (Jackson ImmunoResearch, 001-000-162) filtered through a 0.22-µm filter. At the end of this incubation period, the blocking buffer was replaced with the primary antibody solution (Supplementary Table 5a) in 0.22-µm-filtered antibody dilution buffer (1× PNB, 0.5% Tween and 10% normal donkey serum), and the tissue was incubated at 4 °C overnight in a humidified chamber. Alternatively, slides were labeled with the nuclear detection marker DAPI (Life Technologies, D1306) to record the autofluorescence of the tissue. The slides were then washed with PBS–Tween three times for 5 min each, and the fluorophore-conjugated secondary antibody solution containing DAPI in antibody dilution buffer was added, followed by an incubation period of 1 h in the dark at RT. Staining with secondary antibodies alone on the immediate next tissue section was used as a control. The slides were then washed six times for 10 min each in PBS–Tween and blocked for 1 h, followed by incubation with a directly conjugated antibody for 1 h at RT in a humidified chamber. The slides were then washed two times for 10 min each in PBS–Tween, followed by washing two times with PBS. SlowFade Diamond antifade mountant medium (Invitrogen, S36972) was added to each tissue, and a coverslip (Menzel-Gläser) was carefully mounted. The slides were scanned using the Axio scan.Z1. Following image acquisition, the coverslips were gently removed in PBS. The antibodies were eluted after a 5-min incubation with a freshly prepared tris(2-carboxyethyl) phosphine (TCEP)-based buffer (0.5 M glycine, 3 M guanidium chloride (Carl Roth, 0037.1), 2 M urea (Panreac Applichem ITW reagents, A1360) and 40 mM TCEP (Sigma, C4706) in double distilled water). Following this elution step, the slides were washed with PBS, and the sequential staining procedure was restarted by adding blocking buffer.

Image processing and analysis

Before analysis was performed, the images were processed using ZEN Blue Software. The images were stitched, and the background was subtracted using the rolling ball method with a radius of 75. In addition, autofluorescence was removed by using the signal from the DAPI-only-stained tissue image. The images of multiple staining rounds were then aligned into one single image containing the information for all stained markers. Autofluorescence subtraction and alignment were performed using Python. Image quantification was performed using QuPath[68]. The aligned images were imported and divided into training (40%) and validation (60%) datasets. A 3 × 2 mm region of interest was randomly selected in each training image. Tumor tissue was detected using the pixel classifier RandomTrees trained by selecting the tumor versus non-tumor areas. Training was validated using the validation images and then applied to the complete dataset. A similar approach was used to identify the vessels. The PVN was created by expanding the vessels by 15 µm. Nuclear detection was performed with the StarDist protocol using a cell expansion of 3 (ref. 69). Finally, cell identification was performed using the object classifier RandomTrees for every marker separately. A composite classifier was generated from sequentially added single-marker classifiers to enable final cell identification and exported as a .csv file for downstream analysis with R.

The following were the cells of interest: (1) pTRT cells ($CD45^+$ $CD3^+CD8^+$ T cells double positive for CD103 and PD1), (2) non-pTRT cells ($CD45^+CD3^+CD8^+$ T cells single positive or double negative for CD103 and PD1), (3) MG ($CD45^+CD68^+$ and/or $P2RY12^+CD49D^-$) and (4) MDMs ($CD45^+CD68^+$ and/or $P2RY12^+CD49D^+$).

Only cells with a diameter size of >4 µm and <12.5 µm and a detection probability of >0.65 were kept for the final analysis and visualization.

Ex vivo T cell proliferation assay

Brain tumor tissue was prepared as for bulk RNA-seq. Fresh or thawed dissociated tumor cells (1×10^6 cells per ml) were stained with 1 µl ml^{-1} CFSE (Thermo Fisher Scientific, C34554) in protein-free medium. The cells were stained for 20 min in the dark at RT. Following this incubation period, the remaining CFSE was quenched using complete medium. CFSE-labeled cells (1×10^5) were plated on a flat-bottom, 96-well plate in 100 µl of complete medium. Where indicated, 40 µg ml^{-1} of the blocking anti-PD1 (clone EH12.2H7, BioLegend, 329926) or isotype control (BioLegend, 401401) was added. The cells were incubated at 37 °C and 5% CO_2 for 96 h. Afterward, cells were stained with anti-CD45, anti-CD11B and anti-CD3 (ref. 27), and CFSE dilution in T cells was recorded. All antibodies used in this study are summarized in Supplementary Table 5a. Samples were acquired using a BD LSR Fortessa II, and data analysis was performed with FlowJo software version 10.8.1 (FlowJo).

Statistics and reproducibility

No specific statistical method was used to predetermine sample size, but our cohort sizes are similar or larger than those reported in previous publications[5,7,47,51]. Normality of data distribution was not formally tested, and thus nonparametric statistical analyses were used. No randomization or blinding was performed due to the exploratory nature of the study. Only biological replicates were used for statistical analyses. Summary data are shown in the form of box plots, with the median as center, the 25th and 75th percentiles as the hinges and bounds of the box (first and third quartile) and the upper/lower whiskers extending from the hinge to the largest/smallest value but no further than 1.5× the interquartile range. For bulk RNA-seq, samples with <1,000,000 total counts were excluded. For TCR analysis from bulk RNA-seq, samples with <20 unique TCR sequences were excluded. For FCM analysis, samples with less than 100 cells in the analyzed population were excluded. For IF analysis, tissues with less than 30 total $CD8^+$ T cells were excluded. Statistical analysis was performed with R version 4.0.3 or Prism version 9.3.1 using the test indicated within the corresponding figure caption or sections in the main text. Where relevant, samples were excluded before statistical analysis was performed. When more than two groups were compared, a correction for multiple testing was performed using the Benjamini–Hochberg method.

Reporting summary

Further information on research design is available in the Nature Portfolio Reporting Summary linked to this article.

Data availability

RNA-seq count expression data and scRNA-seq data generated in this study can currently be visualized at https://joycelab.shinyapps.io/braintime/.

Due to strict privacy protection, the raw RNA-seq data will be made available when possible. Future users can contact the corresponding author for access to the raw, unprocessed RNA-seq data, and those requests will then be individually reviewed by the relevant institutional committees. Gene signatures from the MSigDB can be found on the database website (http://www.gsea-msigdb.org/gsea/msigdb). Curated TCR sequences with known antigen specificity were obtained from the VDJdb database (https://vdjdb.cdr3.net/). Published gene signatures for neoantigen-reactive $CD8^+$ T cells are provided in Supplementary

Table 1c. Source data are provided with this paper. All other data supporting the findings of this study are available from the corresponding author upon reasonable request.

Code availability

No custom code was used or developed for the analyses presented in this study. Standard workflows and open-source R packages and software were used (Methods).

References

1. Azzarelli, R., Simons, B. D. & Philpott, A. The developmental origin of brain tumours: a cellular and molecular framework. *Development* **145**, dev162693 (2018).
2. Steindl, A. et al. Changing characteristics, treatment approaches and survival of patients with brain metastasis: data from 6,031 individuals over an observation period of 30 years. *Eur. J. Cancer* **162**, 170–181 (2022).
3. Poon, M. T. C., Sudlow, C. L. M., Figueroa, J. D. & Brennan, P. M. Longer-term (≥2 years) survival in patients with glioblastoma in population-based studies pre- and post-2005: a systematic review and meta-analysis. *Sci. Rep.* **10**, 11622 (2020).
4. Sperduto, P. W. et al. Survival in patients with brain metastases: summary report on the updated diagnosis-specific graded prognostic assessment and definition of the eligibility quotient. *J. Clin. Oncol.* **38**, 3773–3784 (2020).
5. Klemm, F. et al. Interrogation of the microenvironmental landscape in brain tumors reveals disease-specific alterations of immune cells. *Cell* **181**, 1643–1660 (2020).
6. Quail, D. F. & Joyce, J. A. The microenvironmental landscape of brain tumors. *Cancer Cell* **31**, 326–341 (2017).
7. Friebel, E. et al. Single-cell mapping of human brain cancer reveals tumor-specific instruction of tissue-invading leukocytes. *Cell* **181**, 1626–1642 (2020).
8. Tawbi, H. A. et al. Long-term outcomes of patients with active melanoma brain metastases treated with combination nivolumab plus ipilimumab (CheckMate 204): final results of an open-label, multicentre, phase 2 study. *Lancet Oncol.* **22**, 1692–1704 (2021).
9. Goldberg, S. B. et al. Pembrolizumab for management of patients with NSCLC and brain metastases: long-term results and biomarker analysis from a non-randomised, open-label, phase 2 trial. *Lancet Oncol.* **21**, 655–663 (2020).
10. Chan, H. Y., Choi, J., Jackson, C. & Lim, M. Combination immunotherapy strategies for glioblastoma. *J. Neurooncol.* **151**, 375–391 (2021).
11. Le, D. T. et al. PD-1 blockade in tumors with mismatch-repair deficiency. *N. Engl. J. Med.* **372**, 2509–2520 (2015).
12. Marabelle, A. et al. Association of tumour mutational burden with outcomes in patients with advanced solid tumours treated with pembrolizumab: prospective biomarker analysis of the multicohort, open-label, phase 2 KEYNOTE-158 study. *Lancet Oncol.* **21**, 1353–1365 (2020).
13. Mlecnik, B. et al. Comprehensive intrametastatic immune quantification and major impact of immunoscore on survival. *J. Natl Cancer Inst.* **110**, 97–108 (2018).
14. Uryvaev, A., Passhak, M., Hershkovits, D., Sabo, E. & Bar-Sela, G. The role of tumor-infiltrating lymphocytes (TILs) as a predictive biomarker of response to anti-PD1 therapy in patients with metastatic non-small cell lung cancer or metastatic melanoma. *Med. Oncol.* **35**, 25 (2018).
15. Pocha, K. et al. Surfactant expression defines an inflamed subtype of lung adenocarcinoma brain metastases that correlates with prolonged survival. *Clin. Cancer Res.* **26**, 2231–2243 (2020).
16. van der Leun, A. M., Thommen, D. S. & Schumacher, T. N. $CD8^+$ T cell states in human cancer: insights from single-cell analysis. *Nat. Rev. Cancer* **20**, 218–232 (2020).
17. Wu, T. D. et al. Peripheral T cell expansion predicts tumour infiltration and clinical response. *Nature* **579**, 274–278 (2020).
18. Yost, K. E. et al. Clonal replacement of tumor-specific T cells following PD-1 blockade. *Nat. Med.* **25**, 1251–1259 (2019).
19. Liu, B. et al. Temporal single-cell tracing reveals clonal revival and expansion of precursor exhausted T cells during anti-PD-1 therapy in lung cancer. *Nat. Cancer* **3**, 108–121 (2022).
20. Miller, B. C. et al. Subsets of exhausted $CD8^+$ T cells differentially mediate tumor control and respond to checkpoint blockade. *Nat. Immunol.* **20**, 326–336 (2019).
21. Sade-Feldman, M. et al. Defining T cell states associated with response to checkpoint immunotherapy in melanoma. *Cell* **175**, 998–1013 (2018).
22. Leader, A. M. et al. Single-cell analysis of human non-small cell lung cancer lesions refines tumor classification and patient stratification. *Cancer Cell* **39**, 1594–1609 (2021).
23. Litchfield, K. et al. Meta-analysis of tumor- and T cell-intrinsic mechanisms of sensitization to checkpoint inhibition. *Cell* **184**, 596–614 (2021).
24. Zhang, Y. et al. Single-cell analyses reveal key immune cell subsets associated with response to PD-L1 blockade in triple-negative breast cancer. *Cancer Cell* **39**, 1578–1593 (2021).
25. Lowery, F. J. et al. Molecular signatures of antitumor neoantigen-reactive T cells from metastatic human cancers. *Science* **375**, 877–884 (2022).
26. Zheng, L. et al. Pan-cancer single-cell landscape of tumor-infiltrating T cells. *Science* **374**, abe6474 (2021).
27. Maas, R. R. et al. An integrated pipeline for comprehensive analysis of immune cells in human brain tumor clinical samples. *Nat. Protoc.* **16**, 4692–4721 (2021).
28. Guillaumet-Adkins, A. et al. Single-cell transcriptome conservation in cryopreserved cells and tissues. *Genome Biol.* **18**, 45 (2017).
29. Galletti, G. et al. Two subsets of stem-like $CD8^+$ memory T cell progenitors with distinct fate commitments in humans. *Nat. Immunol.* **21**, 1552–1562 (2020).
30. Andreatta, M. et al. Interpretation of T cell states from single-cell transcriptomics data using reference atlases. *Nat. Commun.* **12**, 2965 (2021).
31. Caushi, J. X. et al. Transcriptional programs of neoantigen-specific TIL in anti-PD-1-treated lung cancers. *Nature* **596**, 126–132 (2021).
32. Hanada, K. I. et al. A phenotypic signature that identifies neoantigen-reactive T cells in fresh human lung cancers. *Cancer Cell* **40**, 479–493 (2022).
33. Oliveira, G. et al. Phenotype, specificity and avidity of antitumour $CD8^+$ T cells in melanoma. *Nature* **596**, 119–125 (2021).
34. Simoni, Y. et al. Bystander $CD8^+$ T cells are abundant and phenotypically distinct in human tumour infiltrates. *Nature* **557**, 575–579 (2018).
35. Duhen, T. et al. Co-expression of CD39 and CD103 identifies tumor-reactive CD8 T cells in human solid tumors. *Nat. Commun.* **9**, 2724 (2018).
36. Losurdo, A. et al. Single-cell profiling defines the prognostic benefit of $CD39^{high}$ tissue resident memory $CD8^+$ T cells in luminal-like breast cancer. *Commun. Biol.* **4**, 1117 (2021).
37. Duraiswamy, J. et al. Myeloid antigen-presenting cell niches sustain antitumor T cells and license PD-1 blockade via CD28 costimulation. *Cancer Cell* **39**, 1623–1642 (2021).
38. Jansen, C. S. et al. An intra-tumoral niche maintains and differentiates stem-like CD8 T cells. *Nature* **576**, 465–470 (2019).
39. Brummelman, J. et al. High-dimensional single cell analysis identifies stem-like cytotoxic $CD8^+$ T cells infiltrating human tumors. *J. Exp. Med.* **215**, 2520–2535 (2018).

40. Galon, J. & Bruni, D. Approaches to treat immune hot, altered and cold tumours with combination immunotherapies. *Nat. Rev. Drug Discov.* **18**, 197–218 (2019).
41. Joyce, J. A. & Fearon, D. T. T cell exclusion, immune privilege, and the tumor microenvironment. *Science* **348**, 74–80 (2015).
42. Lohr, J. et al. Effector T-cell infiltration positively impacts survival of glioblastoma patients and is impaired by tumor-derived TGF-β. *Clin. Cancer Res.* **17**, 4296–4308 (2011).
43. Mariathasan, S. et al. TGFβ attenuates tumour response to PD-L1 blockade by contributing to exclusion of T cells. *Nature* **554**, 544–548 (2018).
44. Wang, Z. et al. Carcinomas assemble a filamentous CXCL12–keratin-19 coating that suppresses T cell-mediated immune attack. *Proc. Natl Acad. Sci. USA* **119**, e2119463119 (2022).
45. Lopez de Rodas, M. & Schalper, K. A. Tumour antigen-induced T cell exhaustion—the archenemy of immune-hot malignancies. *Nat. Rev. Clin. Oncol.* **18**, 749–750 (2021).
46. Alexandrov, L. B. et al. Signatures of mutational processes in human cancer. *Nature* **500**, 415–421 (2013).
47. Sudmeier, L. J. et al. Distinct phenotypic states and spatial distribution of $CD8^+$ T cell clonotypes in human brain metastases. *Cell Rep. Med.* **3**, 100620 (2022).
48. Alvisi, G. et al. IRF4 instructs effector T_{reg} differentiation and immune suppression in human cancer. *J. Clin. Invest.* **130**, 3137–3150 (2020).
49. Guldner, I. H. et al. CNS-native myeloid cells drive immune suppression in the brain metastatic niche through CXCL10. *Cell* **183**, 1234–1248 (2020).
50. Uyttenhove, C. et al. Evidence for a tumoral immune resistance mechanism based on tryptophan degradation by indoleamine 2,3-dioxygenase. *Nat. Med.* **9**, 1269–1274 (2003).
51. Gonzalez, H. et al. Cellular architecture of human brain metastases. *Cell* **185**, 729–745 (2022).
52. Liu, B., Zhang, Y., Wang, D., Hu, X. & Zhang, Z. Single-cell meta-analyses reveal responses of tumor-reactive $CXCL13^+$ T cells to immune-checkpoint blockade. *Nat. Cancer* **3**, 1123–1136 (2022).
53. Chowell, D. et al. Improved prediction of immune checkpoint blockade efficacy across multiple cancer types. *Nat. Biotechnol.* **40**, 499–506 (2022).
54. Brummelman, J. et al. Development, application and computational analysis of high-dimensional fluorescent antibody panels for single-cell flow cytometry. *Nat. Protoc.* **14**, 1946–1969 (2019).
55. Dobin, A. et al. STAR: ultrafast universal RNA-seq aligner. *Bioinformatics* **29**, 15–21 (2013).
56. Li, B. & Dewey, C. N. RSEM: accurate transcript quantification from RNA-seq data with or without a reference genome. *BMC Bioinformatics* **12**, 323 (2011).
57. Ritchie, M. E. et al. limma powers differential expression analyses for RNA-sequencing and microarray studies. *Nucleic Acids Res.* **43**, e47 (2015).
58. Chen, Y., Lun, A. T. & Smyth, G. K. From reads to genes to pathways: differential expression analysis of RNA-seq experiments using Rsubread and the edgeR quasi-likelihood pipeline. *F1000Res* **5**, 1438 (2016).
59. Subramanian, A. et al. Gene set enrichment analysis: a knowledge-based approach for interpreting genome-wide expression profiles. *Proc. Natl Acad. Sci. USA* **102**, 15545–15550 (2005).
60. Bolotin, D. A. et al. MiXCR: software for comprehensive adaptive immunity profiling. *Nat. Methods* **12**, 380–381 (2015).
61. Bolger, A. M., Lohse, M. & Usadel, B. Trimmomatic: a flexible trimmer for Illumina sequence data. *Bioinformatics* **30**, 2114–2120 (2014).
62. Shugay, M. et al. VDJtools: unifying post-analysis of T cell receptor repertoires. *PLoS Comput. Biol.* **11**, e1004503 (2015).
63. Hao, Y. et al. Integrated analysis of multimodal single-cell data. *Cell* **184**, 3573–3587 (2021).
64. Bunis, D. G., Andrews, J., Fragiadakis, G. K., Burt, T. D. & Sirota, M. dittoSeq: universal user-friendly single-cell and bulk RNA sequencing visualization toolkit. *Bioinformatics* **36**, 5535–5536 (2020).
65. Hafemeister, C. & Satija, R. Normalization and variance stabilization of single-cell RNA-seq data using regularized negative binomial regression. *Genome Biol.* **20**, 296 (2019).
66. Borcherding, N., Bormann, N. L. & Kraus, G. scRepertoire: an R-based toolkit for single-cell immune receptor analysis. *F1000Res* **9**, 47 (2020).
67. Van Gassen, S. et al. FlowSOM: using self-organizing maps for visualization and interpretation of cytometry data. *Cytometry A* **87**, 636–645 (2015).
68. Bankhead, P. et al. QuPath: open source software for digital pathology image analysis. *Sci. Rep.* **7**, 16878 (2017).
69. Schmidt, U., Weigert, M., Broaddus, C. & Myers, G. Cell detection with star–convex polygons. Preprint at https://doi.org/10.48550/arXiv.1806.03535 (2018).

Acknowledgements

We express our deepest gratitude to all individuals who kindly donated tissue or blood for this study. We thank the Neurosurgery/Neurooncology clinical team of the Centre Hospitalier Universitaire Vaudois, particularly the neurosurgery operating room staff and the technicians at the Pathology Department for their support in coordinating tissue collection. We are grateful to L. B. Bosque and Á. Álvarez-Prado for their technical assistance during sample processing and all current and former members of the Joyce lab for valuable scientific discussions, including F. Klemm and S. Watson. We thank D. Labes, R. Bedel, F. S. de Oyanguren and K. Blackney of the University of Lausanne Flow Cytometry Facility for assistance with cell sorting; A. Tancredi of the Hegi lab for assistance in accessing banked tissue samples; and S. Carmona and D. Gfeller, University of Lausanne, for scientific advice regarding bioinformatic analysis of T cells. This research was supported by the Breast Cancer Research Foundation, Carigest Foundation, Fondation ISREC, Ludwig Institute for Cancer Research and the University of Lausanne (to J.A.J.). K.S. was supported, in part, by an Erwin-Schrödinger Fellowship from the Austrian Science Fund (FWF, J4343-B28). S.G. was supported by Fondation Leenaards and is currently supported, in part, by a Fondation ISREC fellowship. E.L. is a CRI Lloyd J. Old STAR (CRI Award 3914) and is supported by the Associazione Italiana per la Ricerca sul Cancro (AIRC IG 20676 and AIRC 5×1000 UniCanVax 22757). G.G. was supported by the Fondazione Italiana per la Ricerca sul Cancro-Associazione Italiana per la Ricerca sul Cancro (FIRC-AIRC). The purchase of a FACSSymphony A5 was defrayed, in part, by a grant from the Italian Ministry of Health (Agreement 82/2015).

Author contributions

V.W. and J.A.J. designed the study and wrote the manuscript. V.W., R.R.M., K.S., G.G., P.G.A., M.K., S.G., J. Lilja and A.S. performed experiments and/or analyzed data. N.F. and P.W. generated the count matrix for bulk RNA-seq. J. Lourenco and N.F. prepared the BrainTIME v2 portal to access the sequencing data. V.W. performed all other computational analyses and prepared all figures. R.R.M., S.G., A.F.H., R.T.D., M.E.H., A.L., E.V. and M.A. provided clinical material and information. J.-P.B. provided histopathological reviews. E.L. designed experiments, supervised G.G. and A.S. and analyzed data. J.A.J. supervised the study. All authors reviewed, edited or commented on the manuscript.

Funding

Open access funding provided by University of Lausanne.

Competing interests

M.E.H. has an advisory role at TME Pharma. E.L. receives research grants from Bristol Meyers Squibb on a topic unrelated to this manuscript. J.A.J. currently serves on the scientific advisory board of Pionyr Immunotherapeutics and received an honorarium for speaking at a research symposium organized by Bristol Meyers Squibb (last 3 years). All other authors have no competing interests.

Additional information

Extended data is available for this paper at https://doi.org/10.1038/s43018-023-00566-3.

Supplementary information The online version contains supplementary material available at https://doi.org/10.1038/s43018-023-00566-3.

Correspondence and requests for materials should be addressed to Johanna A. Joyce.

Peer review information *Nature Cancer* thanks Arnold Han and the other, anonymous, reviewer(s) for their contribution to the peer review of this work.

Reprints and permissions information is available at www.nature.com/reprints.

Publisher's note Springer Nature remains neutral with regard to jurisdictional claims in published maps and institutional affiliations.

https://doi.org/10.1038/s43018-023-00566-3

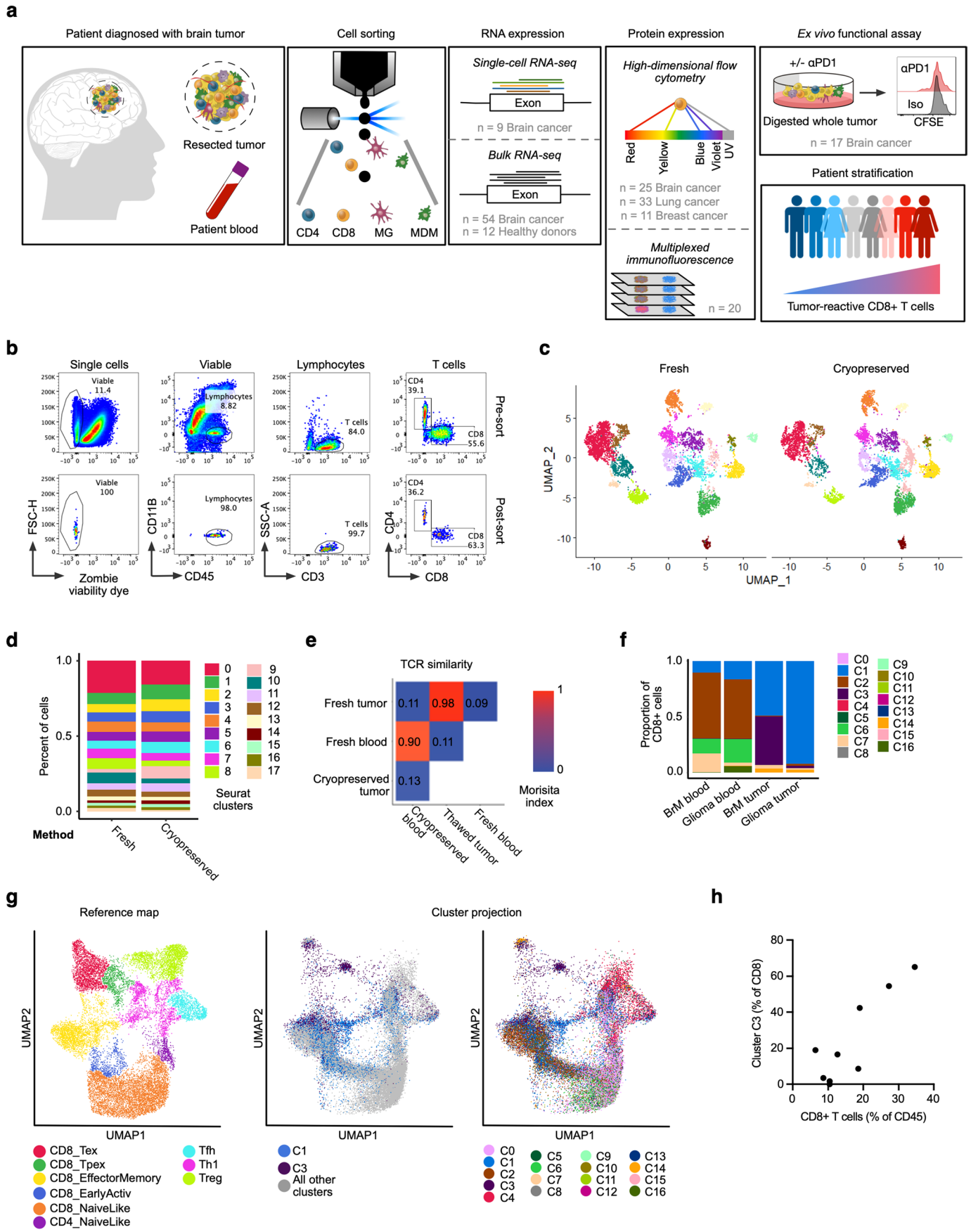

Extended Data Fig. 1 | See next page for caption.

https://doi.org/10.1038/s43018-023-00566-3

Extended Data Fig. 1 | Single-cell RNAseq identifies pTRT in a subset of BrM patients and defines a BrM pTRT-specific gene signature. a, Schematic of the experimental analysis pipeline. **b**, Gating strategy for, and purity of, the sorting of T cells from whole tumor suspensions for single-cell RNAseq. **c**, Representative Uniform Manifold Approximation and Projection (UMAP) of blood and tumor T cells isolated from one patient, before and after cryopreservation. **d**, Stacked bar plots showing the frequency of each cluster before (fresh) and after (frozen) cryopreservation. **e**, Similarity analysis of the TCR repertoire in the blood and tumor of fresh and cryopreserved samples. **f**, Stacked bar plots showing the abundance of CD8 + clusters in BrM and glioma tumors and blood. **g**, Reference map of canonical T cell states (left panel) and projections (right panels) of T cells onto the map colored by cluster identity. **h**, Dot plot showing the relationship between the abundance of cluster C3 among CD8 + T cells and the frequencies of CD8 + T cells among all CD45 + immune cells in nine brain cancer patient samples.

https://doi.org/10.1038/s43018-023-00566-3

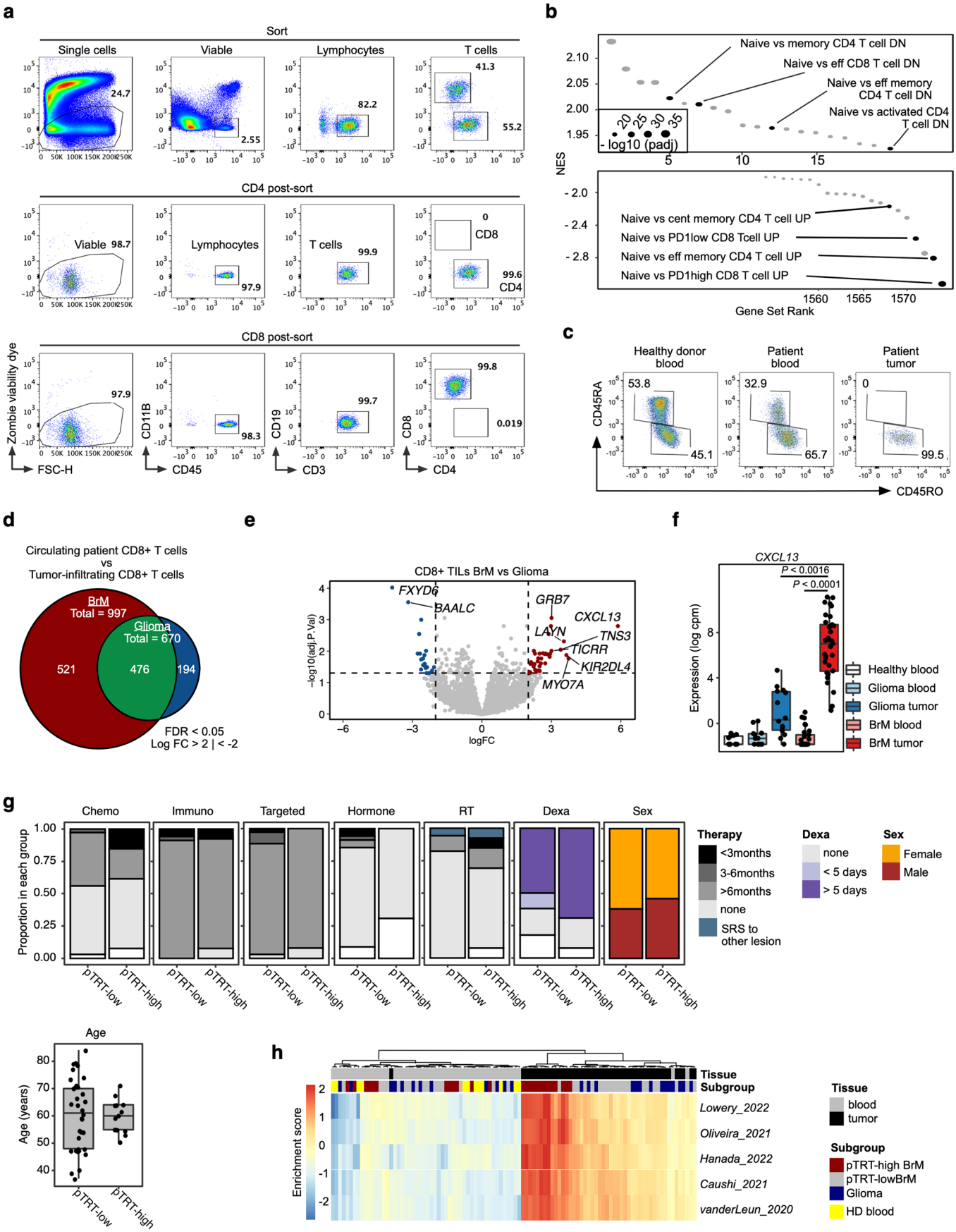

Extended Data Fig. 2 | See next page for caption.

https://doi.org/10.1038/s43018-023-00566-3

Extended Data Fig. 2 | T cell activation and differentiation is a common feature of brain tumor-infiltrating T cells. a, Gating strategy to sort T cells from whole tumor for bulk RNA-seq and control of sorting purity. **b**, The most-enriched pathways in tumor or blood T cells from MSigDB C7 collection are shown. Pathways from (Fig. 2b) are highlighted. For full pathway list, see Supplementary Table 2b. **c**, Representative flow cytometry (FCM) plots showing the expression of CD45 isoforms in blood and tumor T cells. **d**, Venn diagram highlighting the private and shared differentially expressed genes (DEG) from the comparison of matched blood CD8 + T cells versus CD8 + tumor-infiltrating lymphocytes (TILs) using the indicated statistical cutoffs. **e**, Log2(fold-change) versus -log10(adjusted p value) volcano plot showing differential expression analysis contrasting CD8 + TILs from BrM to CD8 + TILs from glioma calculated with *limma* package in *R*. DEG with log2(fold-change) > 3 or log2(fold-change) < -3 and *P.adj* < 0.05 are highlighted. **f**, Box plots showing normalized RNA expression of *CXCL13* as log2(cpm) in CD8 + T cells from blood ($n_{healthy} = 9$, $n_{glioma} = 9$, $n_{BrM} = 25$), or tumor tissue ($n_{glioma} = 14$, $n_{BrM} = 33$). Adjusted *P*-values (Benjamini & Hochberg method) were calculated with *limma* package in *R*. **g**, Stacked bar plots visualizing clinical factors of the n = 47 patients grouped in Fig. 2f. No statistically significant differences between the pTRT-high and the pTRT-low group were observed with respect to patient treatment history, sex, or age (lower left panel). **h**, Heatmap of gene set variation analysis (GSVA) results of five neoantigen-reactive T cell gene signatures in CD8 + T cells isolated from tumors, matched patient blood, and healthy donor blood. Columns and rows are hierarchically clustered. For **f** and **g**, the box plots represent first and third quartiles with median as center; whiskers show 1.5 × interquartile range of the 25th and 75th percentiles.

https://doi.org/10.1038/s43018-023-00566-3

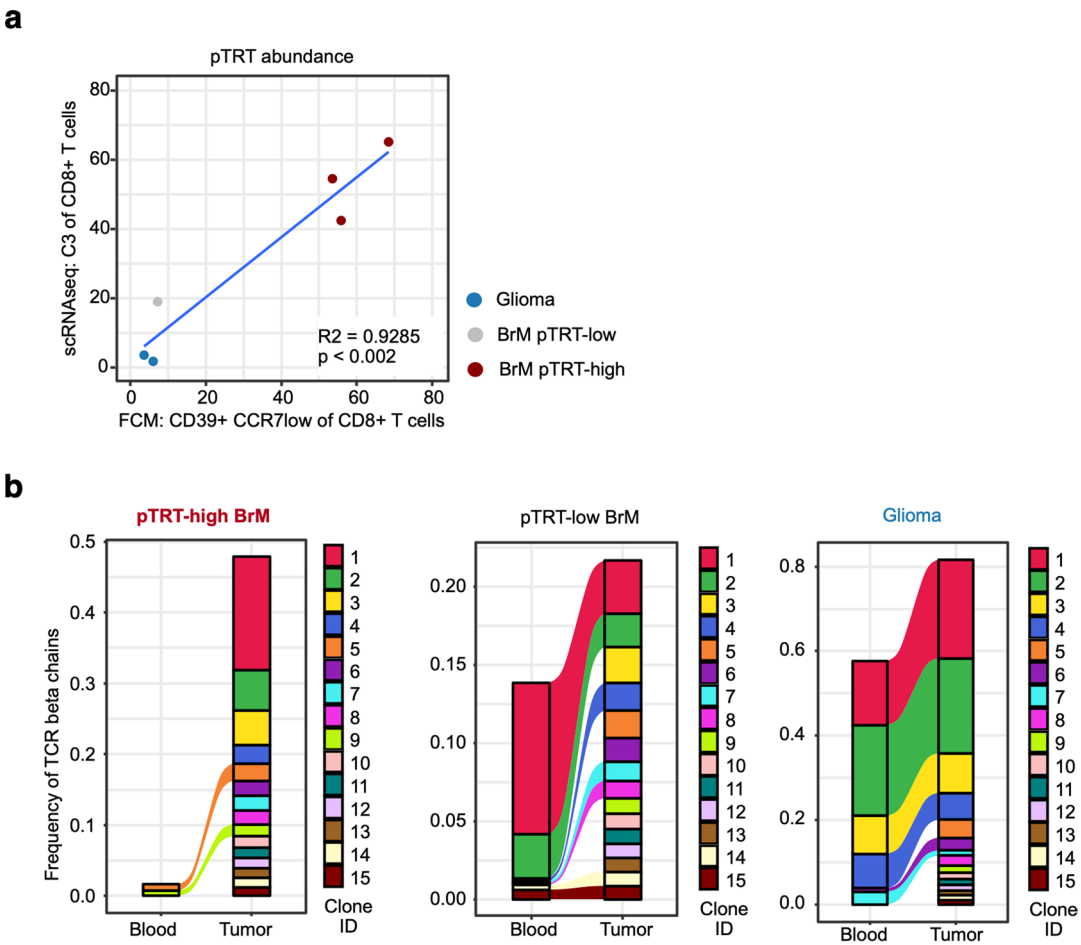

Extended Data Fig. 3 | CD8 + pTRT are expanded predominantly in tumor tissue and can be detected by flow cytometry as CD39 + CCR7low cells. **a**, Dot plot showing the relationship between the abundance of cluster C3 among CD8 + T cells and the frequencies of CD39 + CCR7low cells among all CD8 + T cells in six brain tumors profiled by FCM and scRNA-seq. Significance determined with linear regression. **b**, CD8 + T cells in pTRT-high tumors are highly abundant and clonally expanded. Representative alluvial plots visualizing the frequency of the top 15 T cell receptor (TCR) clones within three patients (pTRT-high BrM, pTRT-low BrM, and a glioma patient) in the blood and tumor, respectively. Each clone within an individual patient sample is annotated with a unique color.

https://doi.org/10.1038/s43018-023-00566-3

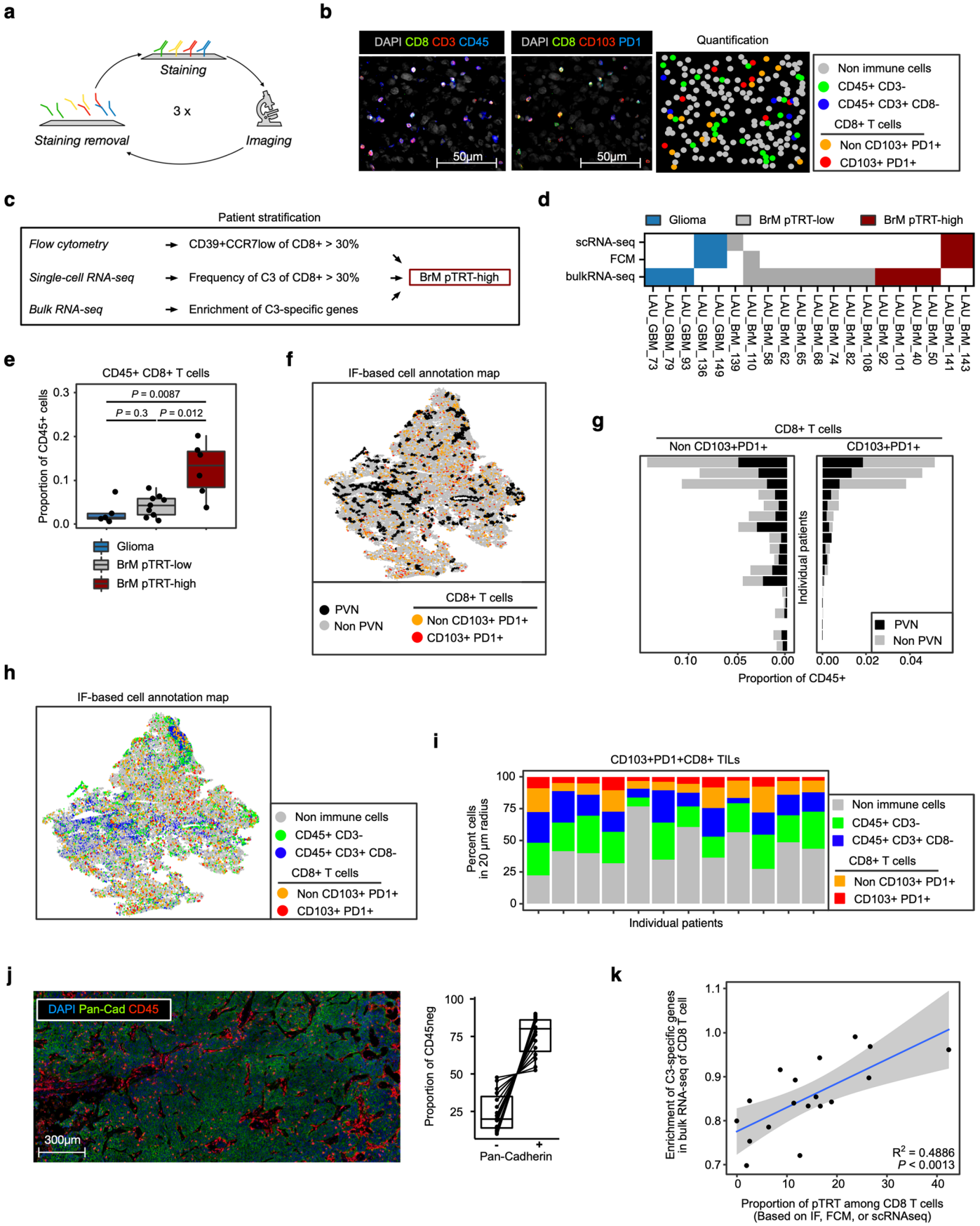

Extended Data Fig. 4 | See next page for caption.

https://doi.org/10.1038/s43018-023-00566-3

Extended Data Fig. 4 | pTRT in BrM are located in perivascular niches, stroma, and within tumor nests. a, Schematic of multiplexed immunofluorescence (IF) imaging. **b**, Representative IF images and quantification using QuPath and R software from one patient are shown. **c**, Patient stratification strategy for IF analysis based on FCM, scRNA-seq, and bulk RNA-seq data. **d**, Heatmap summarizing the pTRT status for each patient using the strategy described in (c). **e**, Box plot showing the abundance of CD8 + T cells in tumors ($n_{glioma} = 5$, $n_{BrM\_pTRT\text{-}low} = 9$, and $n_{BrM\_pTRT\text{-}high} = 6$) as the proportion of all CD45 + immune cells detected by IF. Significance determined with unpaired two-sided Wilcoxon-test with Benjamini-Hochberg multiple comparison correction. **f**, Full section with IF-derived cell annotation of the indicated populations and tissue regions for one representative patient sample. **g**, Stacked bar plots showing the quantification of the location of CD103 + PD1 + CD8 + TILs and all other CD8 + TILs in each individual patient. Color indicates the location within (perivascular niches, PVN) or outside (non-PVN) a 15 µm radius surrounding the nearest vessel. **h**, Full section IF-derived annotation of the indicated cell populations for one representative patient sample. **i**, Neighborhood analysis summarizing the cell types within a 20 µm radius around CD103 + PD1 + CD8 + TILs in individual patients with > ten CD103 + PD1 + CD8 + cells in each analyzed tissue section. **j**, Representative image (left panel) and quantification (right panel) of the proportion of tumor cells (pan-cadherin +) among all CD45neg non-immune cells in n = 19 brain metastasis samples. **k**, Dot plot showing the relationship between the enrichment of C3-specific genes in CD8 + T cells profiled by bulk RNA-seq and the frequencies of pTRT measured by IF, FCM, and scRNA-seq. Significance determined with linear regression. Confidence interval of 0.95 is indicated in grey. For **e** and **j**, the box plots represent first and third quartiles with median as center; whiskers show 1.5 × interquartile range of the 25th and 75th percentiles.

https://doi.org/10.1038/s43018-023-00566-3

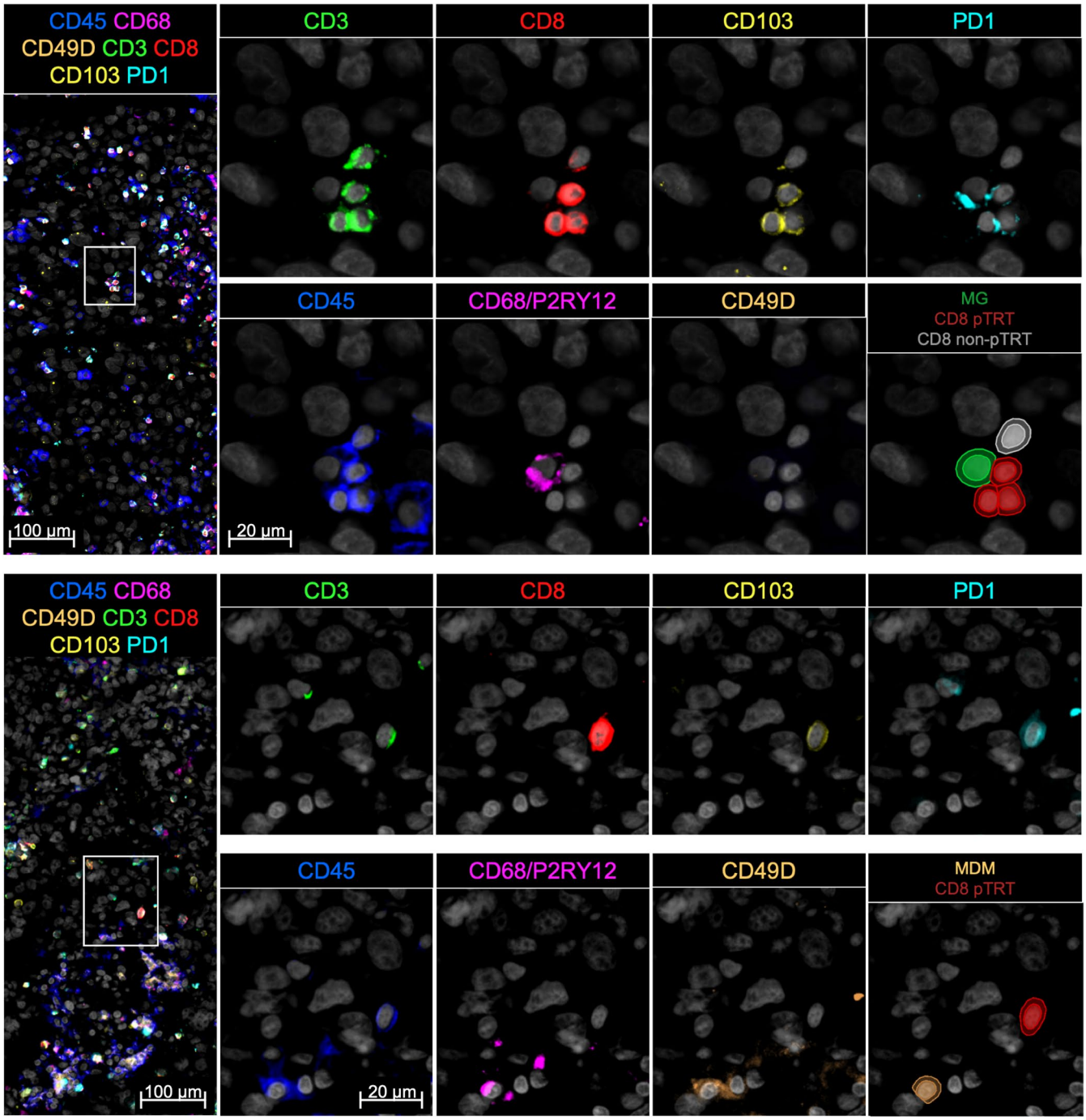

Extended Data Fig. 5 | Distance of myeloid cells to CD8 + TILs. Representative IF images and quantification using QuPath and R software from two patients are shown, indicating T cells, MG (upper set of images) and MDMs (lower set of images).

https://doi.org/10.1038/s43018-023-00566-3

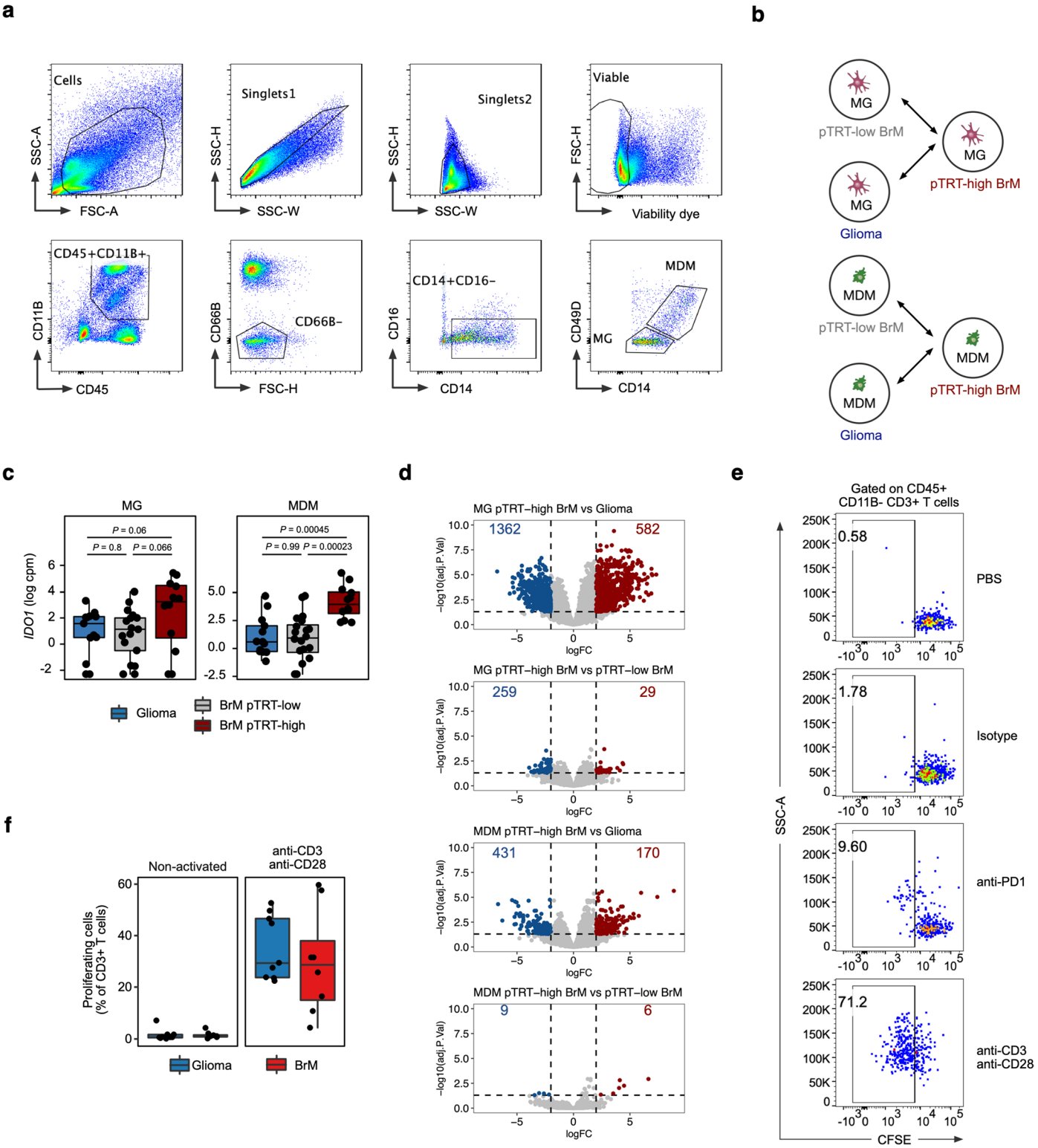

Extended Data Fig. 6 | Myeloid cells with antigen-presentation capacity are associated with high pTRT abundance. a, Gating strategy to sort MG and MDM from whole tumors for bulk RNA-seq. **b**, Schematic of the differential expression analysis (DEA). **c**, Box plots showing expression of *IDO1* as log2(cpm) in $n_{MG} = 42$ and $n_{MDM} = 45$ patients. Adjusted *P*-values (Benjamini & Hochberg method) were calculated with *limma* package in *R*. **d**, Log2(fold-change) versus -log10(adjusted *P*-value, Benjamini & Hochberg method) volcano plot showing DEA results contrasting MG or MDMs from pTRT-high BrM to respective cells in pTRT-low BrM or glioma tumors calculated with *limma* package in *R*. Number of DEG using log2(fold-change) > 2 or log2(fold-change) < -2 and *P.adj* < 0.05 as cutoff are indicated. For full gene lists, see Supplementary Table 3b. **e**, Representative FCM plots showing CFSE dilution in CD3 + cells from one tumor sample under the experimental conditions indicated. Percentage of proliferating T cells is annotated for each panel. **f**, Box plots summarizing the proliferation of T cells isolated from n = 9 glioma or n = 8 BrM tumors, respectively, with or without anti-CD3/anti-CD28 stimulation. For **c** and **f**, the box plots represent first and third quartiles with median as center; whiskers show 1.5 × interquartile range of the 25th and 75th percentiles.

https://doi.org/10.1038/s43018-023-00566-3

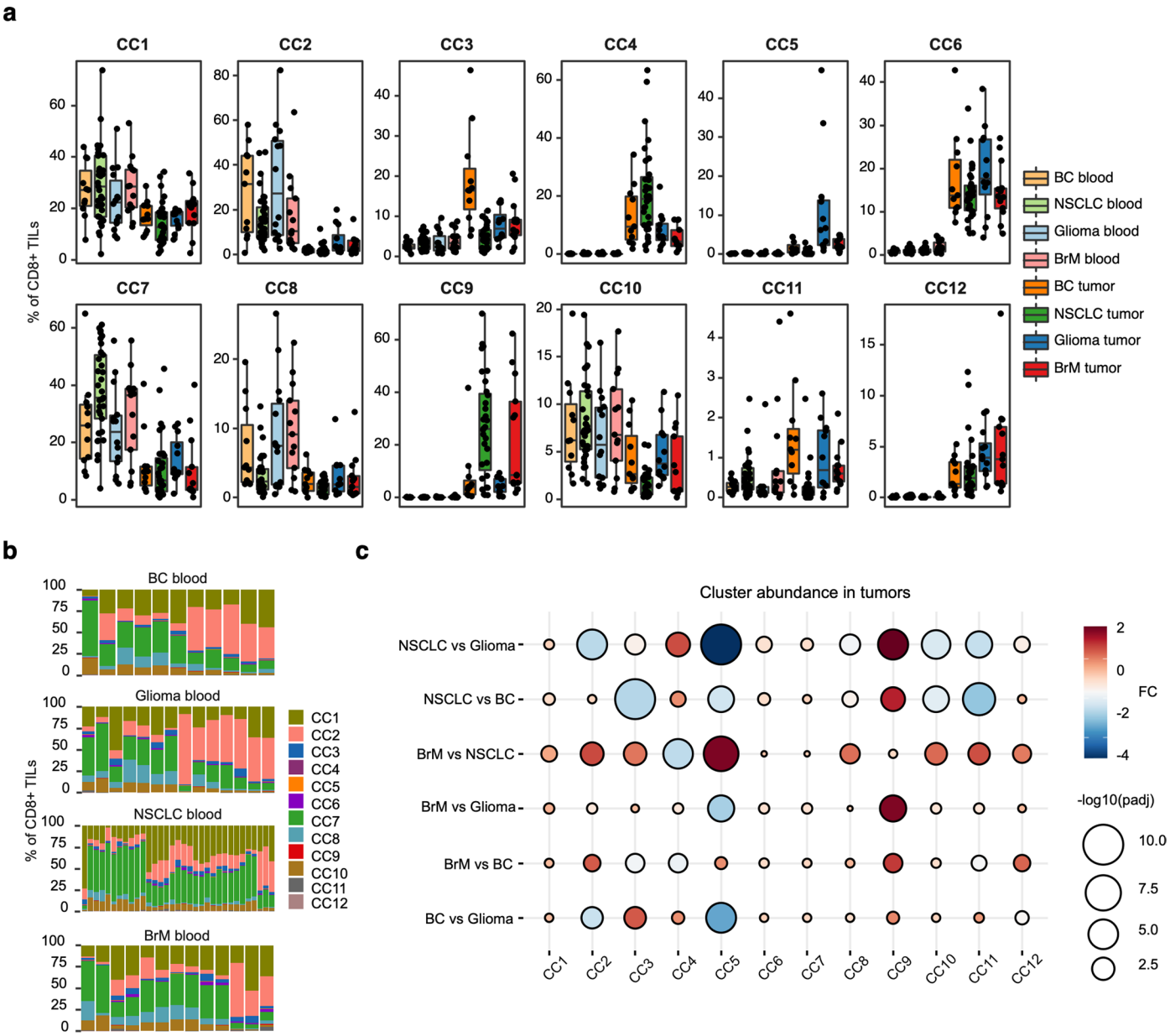

Extended Data Fig. 7 | Abundance of pTRT in BrM and primary NSCLC is comparable, while the phenotypes are distinct. a, Abundance of each cytometry cluster (CC) in the blood and tumor of $n_{BC} = 11$, $n_{NSCLC} = 30$, $n_{glioma} = 12$, and $n_{BrM} = 13$ patients. **b**, Stacked bar plots showing the abundance of each CC in individual patient blood samples grouped by the disease. **c**, Balloon plot summarizing the differences in the abundance of each cluster in tumors of the four disease groups. Balloon size represents the -log10(adjusted p value), and the color indicates the fold change. For **a**, the box plots represent first and third quartiles with median as center; whiskers show 1.5 × interquartile range of the 25th and 75th percentiles.

nature portfolio

Corresponding author(s): Johanna A. Joyce

Last updated by author(s): Apr 6, 2023

Reporting Summary

Nature Portfolio wishes to improve the reproducibility of the work that we publish. This form provides structure for consistency and transparency in reporting. For further information on Nature Portfolio policies, see our Editorial Policies and the Editorial Policy Checklist.

Statistics

For all statistical analyses, confirm that the following items are present in the figure legend, table legend, main text, or Methods section.

n/a	Confirmed
☐	☒ The exact sample size (*n*) for each experimental group/condition, given as a discrete number and unit of measurement
☐	☒ A statement on whether measurements were taken from distinct samples or whether the same sample was measured repeatedly
☐	☒ The statistical test(s) used AND whether they are one- or two-sided *Only common tests should be described solely by name; describe more complex techniques in the Methods section.*
☒	☐ A description of all covariates tested
☐	☒ A description of any assumptions or corrections, such as tests of normality and adjustment for multiple comparisons
☐	☒ A full description of the statistical parameters including central tendency (e.g. means) or other basic estimates (e.g. regression coefficient) AND variation (e.g. standard deviation) or associated estimates of uncertainty (e.g. confidence intervals)
☐	☒ For null hypothesis testing, the test statistic (e.g. *F*, *t*, *r*) with confidence intervals, effect sizes, degrees of freedom and *P* value noted *Give P values as exact values whenever suitable.*
☒	☐ For Bayesian analysis, information on the choice of priors and Markov chain Monte Carlo settings
☒	☐ For hierarchical and complex designs, identification of the appropriate level for tests and full reporting of outcomes
☒	☐ Estimates of effect sizes (e.g. Cohen's *d*, Pearson's *r*), indicating how they were calculated

Our web collection on statistics for biologists contains articles on many of the points above.

Software and code

Policy information about availability of computer code

Data collection

Flow Cytometry data were collected on a BD Fortessa or BD FACSymphony A5 equipped with FACSDiva software version 8.0.1 (BD Biosciences). Cell sorting was performed on a BD AriaIII. Immune cell populations were sorted based on the markers and gating strategy described in (Maas, R. R. et al. Nature Protocols, 2021).
For bulk RNA sequencing, RNA extraction, library preparation and sequencing of sorted populations was performed at Genewiz Services (http://www.genewiz.com/) using the Ultra-Low Input RNA-Seq service which utilizes a Poly(A) selection with enrichment for full-length transcripts. Paired-end sequencing of the libraries was performed using the Illumina HiSeq instrument with 2x150 bp configuration. Raw sequencing reads were aligned to a reference human genome using STAR v2.7.7a and counts were quantified using RSEM v1.3.3. Human genome version 38 was used with GENCODE v36 annotation. Raw counts of transcripts with the same gene symbol were pooled. Samples with <1,000,000 total counts were excluded.
For single cell RNA sequencing, a maximum of 16,000 sorted T cells were loaded onto the 10x Chromium Controller following the manufacturer's instruction manual. For the generation of Gel Beads in Emulsion (GEM), Chromium Next GEM Single Cell 5' Kit v2 (10x, 1000263) and the Chromium Next GEM Chip K Single Cell Kit (10x, 1000287) were used. Gene expression (GEX) and T cell receptor (VDJ) libraries were prepared using the Library Construction Kit (10x, 1000190) and Chromium Single Cell Human TCR Amplification Kit (10x, 1000252), respectively, following the manufacturer's instruction manual. Library quantity and quality were determined using Qubit Fluorometric Quantification (Thermo Fisher Scientific, Q32851) and High Sensitivity Next-Generation-Sequencing Fragment Analysis (Agilent Technologies, DNF-474-0500). Sequencing was performed by Genewiz Services (http://www.genewiz.com/) on an Illumina NovaSeq6000 S4 Flow Cell using a 10x sequencing configuration. Targeted sequencing depth was >20'000 reads/cell for GEX and >5'000 reads/cell for VDJ libraries, respectively.
Immunofluorescence stainings of tissues were acquired with Zeiss Axio Scan.Z1 (Zeiss Germany) with ZEN software version 3.1 .

Data analysis

All bioinformatic analyses were performed within the R environment version 4.0.3 and Bioconductor version 3.12. Statistical analysis was performed in R (v. 4.0.3) or Prism version 9.3.1.

For bulk RNA Seq data, RSEM counts of T cells were processed to account for potential contamination with transcriptionally highly active tumor cells (sorted as CD45-negative cells). A four step process was applied for each disease group, respectively: a) Selecting 250 genes with highest absolute expression in CD45-negative cells; b) Performing differential expression analysis (DEA) between CD45-negative cells and all T cells (blood and tumor) using the limma (v. 3.46.0) (RRID:SCR_010943) package; c) Identifying genes expressed at substantially higher levels in CD45-negative cells compared to T cells using very stringent cutoffs with fold change > 3 and FDR < 0.001. d) Generating overlap between differentially expressed genes (DEG) from (c) and highly expressed tumor cell-specific genes from (a). The resulting genes (a total of 136) were removed from the count matrix (Supplementary Table 5b). Differential expression analysis of bulk RNA Seq data was performed with limma in R. Pathway enrichment in sample groups was analyzed by gene set enrichment analysis using the fgsea (v. 1.16.0) (RRID:SCR_020938) package, considering pathways with a minimum size of 15 and maximum size of 500 genes. Gene ranks for fgsea were derived from the t-statistic of limma. Pathway enrichment in individual samples was analyzed by gene set variation analysis (GSVA, v. 1.38.2) using the gsva method and variance stabilized counts as input.

To derive individual TCR beta chain sequences from our bulk RNAseq data, the mixcr (v. 3.0.12) framework (Bolotin, D. A. et al. 2015) was used with default parameters. Briefly, the raw reads were cleaned from adapter sequences using Trimmomatic (v. 0.39) (Bolger, A. M., Lohse, M. & Usadel, B. 2014) and duplicated reads were removed with the clumpify function from bbmap (v 39.01) (RRID:SCR_016965). Processed reads were aligned against the reference V, D, J and C genes of the T cell receptor (downloaded September 2019). Aligned reads were quantified and identical reads were summarized into clonotypes. Here, only the TCR beta chain was used and samples with less than 20 unique TCRs were excluded. The diversity of the TCR pools was evaluated with the vdj tools framework (v. 1.2.1) (Shugay, M. et al. 2015) and the Chao estimate was used to determine the lower bound total diversity estimates (Chao 1 index).

For the analysis of single cell RNAseq, FastQ files of the GEX and VDJ libraries were aligned to the human reference genome GRCh38 2020-A (release July 7, 2020) and to the GRCh38 _alts_ensemble-5.0.0, respectively, using cell ranger software (version 6.0) from 10x Genomics. Downstream analysis was performed using Seurat (RRID:SCR_016341) package version 4.0 in R. For visualization, Seurat, dittoSeq (v. 1.10.0) (Bunis, D. G. et al. 2020) and tidyverse (v. 1.3.0) (RRID:SCR_019186) packages were used. For quality control, we retained only cells with < 10% mitochondrial RNA and 250-3000 total features. Samples were integrated with the SCTransform function (Hafemeister, C. & Satija, R. 2019) using the day of sample sorting as the batch parameter. Clustering was performed with 31 dimensions in FindNeighbors and RunUMAP functions and a resolution of 0.18 in the FindClusters function. Cluster-specific genes were identified using the FindMarkers function with FC > 0.25 and at least 25% of cells in each cluster expressing the DEG utilizing the wilcox test. Results were validated by Receiver Operating Characteristic (ROC) analysis in Seurat. Signature scores were calculated using the AddModuleScore function. DEA between groups was performed using the FindMarkers function with the poisson generalized linear model including batch as a covariant. VDJ libraries were processed with the scRepertoire package (v. 1.8.0) (Borcherding, N. et al. 2020). TCR similarity analysis was performed with the clonalOverlap function using the Morisita index.The VDJmatch software version 1.3.1 was used to match TCR beta repertoires (generated by scRNA-seq) against TCR sequences with known antigen specificity. The function match was used with default parameters to align TCR sequences for each CD8+ T cell cluster separately. Results were filtered using the vdjdb.score including matching sequences only with vdjdb.score ≥ 1. Unique matching viral antigens were counted and plotted.

For the analysis of high-dimensional flow cytometry (FCM) data, Flow cytometry standard (FCS) 3.0 files were imported into FlowJo software version 9 (FlowJo LLC). A conventional gating strategy was used to remove aggregates and dead cells. Viable CD3+CD8+ T cells were exported and used for downstream analysis. FlowJo software version 10.8.1 (FlowJo LLC) was used for all analysis requiring manual gating. For unsupervised clustering analysis, samples with < 100 CD8+ T cells were excluded. Remaining samples were down-sampled to 1,500 cells with random sampling and imported into R using the flowCore (v. 2.2.0) and CATALYST (1.14.1) packages (RRID:SCR_002205). Data were transformed with arcsinh-transformation using a cofactor of 150. The flowSOM algorithm was used to cluster the cells (Van Gassen, S. et al. 2015). For clustering, all markers were used with the exception of the live/dead dye, CD3, CD4, CD8 and FOXP3. Visual investigation of the different cluster numbers determined 12 as the most informative parameter. UMAP projections were calculated with the runDR function from CATALYST.

For the analysis of sequential immunofluorescence (IF) staining, images were stitched and the background was subtracted using the rolling ball method with a radius of 75. In addition, autofluorescence was removed by using the signal from the DAPI-only stained tissue image. The images from multiple sequential staining rounds were then aligned into one single image containing the information for all stained markers. The autofluorescence subtraction and the alignment were performed using Python version 3.9.5. Image quantification was performed using QuPath version 0.3.2 (Bankhead, P. et al. 2017). The aligned images were imported and divided into training (40%) and validation (60%) datasets. Tumor tissue was detected using the pixel classifier trained by selecting the tumor vs non-tumor areas. The training was validated using the validation images and then applied to the complete dataset. Nuclear detection was performed with the StarDist protocol using a cell expansion of 3 (Schmidt, U. et al. 2018). A similar approach was used to identify the blood vessels. The perivascular niche (PVN) was created by expanding the vessels by 15µm. Finally, cell identification was performed using the object classifier for every marker separately. The training was validated before it was applied to the complete dataset. A composite classifier was generated from sequentially added single-marker-classifiers to enable final cell identification and exported as a .csv file for downstream analysis with R. Only cells with a diameter size of >4µm and <12.5µm, and a detection probability >0.65, were kept for the final analysis and visualization.

For manuscripts utilizing custom algorithms or software that are central to the research but not yet described in published literature, software must be made available to editors and reviewers. We strongly encourage code deposition in a community repository (e.g. GitHub). See the Nature Portfolio guidelines for submitting code & software for further information.

Data

Policy information about availability of data

All manuscripts must include a data availability statement. This statement should provide the following information, where applicable:

- Accession codes, unique identifiers, or web links for publicly available datasets
- A description of any restrictions on data availability
- For clinical datasets or third party data, please ensure that the statement adheres to our policy

RNA-seq count expression data and single-cell RNAseq data generated in this study can currently be visualized at:
http://sib-pc17.unil.ch:3880/BrainTIME_v2/
Username:JoyceLab
Password: braintimev2_joycelab_2022
Due to patient privacy protection, the raw RNA-seq data will be made available upon request. Gene signatures from the MSigDB can be found on the database website (http://www.gsea-msigdb.org/gsea/msigdb). Curated TCR sequences with known antigen specificity were obtained from the VDJdb database (https://vdjdb.cdr3.net/). Published gene signatures for neoantigen-reactive CD8+ T cells are provided in Supplementary Table 1c. Source data have been provided as Source Data files. All other data supporting the findings of this study are available from the corresponding author upon reasonable request.

Human research participants

Policy information about studies involving human research participants and Sex and Gender in Research.

Reporting on sex and gender	The sex information from all participants has been collected and consent has been obtained for reporting. The sex information was obtained based on self-report.
Population characteristics	Details on human samples can be found in Supplementary Table 1a and 4. The complete brain cancer patient cohort is comprised of n=84 patient specimens as follows: Glioma n=36 (53% male and 47% female, median age: 56 years) Brain metastasis: n=48 (42% male and 58% female, median age: 62 years) The complete cohort of patient with extra-cranial tumors is comprised of n=45 patient specimens as follows: Non-small cell lung cancer: n=34 (53% male and 47% female, mean age: 69.5 years) Breast cancer: n=11 (100% female, median age: 66.18 years)
Recruitment	Samples from brain cancer patients were collected at the Centre Hospitalier Universitaire Vaudois (CHUV, Lausanne, Switzerland). Samples from patients with extra-cranial cancers were collected at Humanitas Hospital (Milan, Italy).
Ethics oversight	The collection of tumor and non-tumor tissue and blood samples from patients with brain disease at the Biobank of the Brain and Spine Tumor Center (BB_031_BBLBGT) of the Centre Hospitalier Universitaire Vaudois (CHUV, Lausanne, Switzerland) was approved by the Commission Cantonale d'éthique de la recherche sur l'être humain (CER-VD, protocol PB 2017-00240, F25 / 99). The use of human samples from patients with extracranial disease was approved by the Humanitas Clinical and Research Center Institutional Review Board (Milan, Italy) under the following protocols: lung cancer tissue and blood samples from patients with non-small cell lung cancer (1501) and breast cancer tissue and blood from patients with breast cancer (ONC-OSS-02-2017).

Note that full information on the approval of the study protocol must also be provided in the manuscript.

Field-specific reporting

Please select the one below that is the best fit for your research. If you are not sure, read the appropriate sections before making your selection.

☒ Life sciences ☐ Behavioural & social sciences ☐ Ecological, evolutionary & environmental sciences

For a reference copy of the document with all sections, see nature.com/documents/nr-reporting-summary-flat.pdf

Life sciences study design

All studies must disclose on these points even when the disclosure is negative.

Sample size	No specific statistical method was used to predetermine sample size, but our cohort sizes are similar or larger than those reported in previous publications studying primary and metastatic human brain cancer which were able to show statistically significant results with their cohorts.
Data exclusions	Bulk RNAseq: Samples with <1,000,000 total counts were excluded. For TCR analysis, samples with <20 unique TCR sequences were excluded. Flow cytometry: Samples with less than 100 cells in the analyzed population were excluded.

	Immunofluorescence: Tissues with less than 30 CD8+ T cells were excluded. Samples were excluded before statistical analysis was performed.
Replication	Each condition/group in the RNAseq, flow cytometry, immunofluorescence staining, and functional analysis contained > 3 independent patient samples. The exact sample sizes are indicated in the figure legends. The in vitro assay was repeated multiple times with independent tissue donors. Immunofluorescence staining images are representatives of multiple replicates from the respective experimental group. While individual bulk RNAseq, single cell RNAseq, flow cytometry, immunofluorescence, and ex vivo functional assays could not all be repeated due to limited size of available material, the core results from each method are completely in line with each other. Thus, each method represents an independent validation of the reproducibility of the main results in this study.
Randomization	Does not apply to this study because it is an exploratory and retrospective analysis of surgically resected brain tumor samples. Tissue was obtained and analyzed as it became available and was sufficient in size.
Blinding	Since this study is an exploratory and retrospective analysis of surgically resected tumor samples, blinding was not required. Moreover, bio-informatics analysis was performed using automated analysis tools described here and in the Methods section.

Reporting for specific materials, systems and methods

We require information from authors about some types of materials, experimental systems and methods used in many studies. Here, indicate whether each material, system or method listed is relevant to your study. If you are not sure if a list item applies to your research, read the appropriate section before selecting a response.

Materials & experimental systems

n/a	Involved in the study
☐	☒ Antibodies
☒	☐ Eukaryotic cell lines
☒	☐ Palaeontology and archaeology
☒	☐ Animals and other organisms
☒	☐ Clinical data
☒	☐ Dual use research of concern

Methods

n/a	Involved in the study
☒	☐ ChIP-seq
☐	☒ Flow cytometry
☒	☐ MRI-based neuroimaging

Antibodies

Antibodies used

All antibodies used in this study are summarized in Supplementary Table 5a.
Information below includes: ANTIBODY; FLUOROCHROME; DILUTION; CLONE; SOURCE; IDENTIFIER; RRID(where available).

Flow cytometry:
Anti-human CD8 BUV805 1:166 SK1 BD Biosciences Cat # 564912 RRID:AB_2744465
Anti-human CD45RO BV570 1:40 UCHL1 BioLegend Cat # 304226 RRID:AB_2563818
Anti-human CD4 BUV615 1:3,333 SK3 BD Biosciences Cat # 624297 N/A
Anti-human CD3 BUV496 1:40 UCHT1 BD Biosciences Cat # 564809 RRID:AB_2744388
Anti-human CCR7 PE-CF594 1:40 150503 BD Biosciences Cat # 562381 RRID:AB_11153301
Anti-human CD28 BV785 1:166 CD28.2 BioLegend Cat # 302950 RRID:AB_2632607
Anti-human CD25 BUV563 1:160 2A3 BD Biosciences Cat # 612918 RRID:AB_2870203
Anti-human CD69 BUV737 1:322 FN50 BD Biosciences Cat # 564439 RRID:AB_2722502
Anti-human CD127 PE-Cy5 1:40 eBioRDR5 eBioscience Cat # 15-1278-42 RRID:AB_2043801
Anti-human PD-1 BV480 1:27 EH12.1 BD Biosciences Cat # 566112 RRID:AB_2739514
Anti-human HLA-DR BUV661 1:166 G46-6 BD Biosciences Cat # 565073 RRID:AB_2722500
Anti-human CD38 BV711 1:166 HIT2 BioLegend Cat # 303528 RRID:AB_2563811
Anti-human CD103 BV421 1:166 Ber-ACT8 BioLegend Cat # 350213 RRID:AB_2563513
Anti-human CD161 BV605 1:20 HP-3G10 BioLegend Cat # 339916 RRID:AB_2563607
Anti-human Granzyme B APC-R700 1:80 GB11 BD Biosciences Cat # 561016 RRID:AB_2033973
Anti-human Granzyme K PE 1:166 GM6C3 Santa Cruz Cat # sc-56125 PE RRID:AB_2263772
Anti-human T-bet PE-Cy7 1:666 4-B10 eBioscience Cat # 25-5825-82 RRID:AB_11042699
Anti-human ICOS BUV395 1:80 DX29 BD Biosciences Cat # 564777 RRID:AB_2738946
Anti-human TIM3 BV650 1:160 7D3 BD Biosciences Cat # 565564 RRID:AB_2722547
Anti-human CD39 APC-Cy7 1:80 A1 BioLegend Cat # 328226 RRID:AB_2571981
Anti-human CXCL13 APC 1:80 53610 Thermo Fisher Cat # MA5-23629 RRID:AB_2610225
Anti-human Ki67 FITC 1:20 B56 BD Biosciences Cat # 556026 RRID:AB_396302
Anti-human FoxP3 PE-Cy5.5 1:40 PCH101 eBioscience Cat # 35-4776-42 RRID:AB_11218682
anti-human-CD45 AF700 1:640 HI30 BioLegend Cat#304024 RRID:AB_493761
anti-mouse/human-CD11B BV421 1:1280 M1/70 BioLegend Cat#101251 RRID:AB_2562904
anti-human-CD66B PE 1:200 G10F5 BioLegend Cat#305106 RRID:AB_2077857
anti-human-CD14 AF488 1:640 HCD14 BioLegend Cat#325610 RRID:AB_830683
anti-human-CD16 BUV737 1:640 3G8 BD Biosciences Cat#612786 RRID:AB_2833077
anti-human-CD49D APC 1:320 9F10 BioLegend Cat#304308 RRID:AB_2130041
anti-human-CD11C BV605 1:320 3.9 BioLegend Cat#301636 RRID:AB_2563796
anti-human-HLA-DR BV711 1:320 L243 BioLegend Cat#307644 RRID:AB_2562913

anti-human-CD3 PerCP/Cy5.5 1:80 HIT3a BioLegend Cat#300328 RRID:AB_1575008
anti-human-CD4 BV650 1:200 OKT4 BioLegend Cat#317436 RRID:AB_2563050
anti-human-CD25 PE 1:80 BC96 BioLegend Cat#302606 RRID:AB_314276
anti-human-CD127 BV510 1:160 A019D5 BioLegend Cat#351332 RRID:AB_2562304
anti-human-CD8A PE/Cy7 1:320 HIT8a BioLegend Cat#300914 RRID:AB_314118
anti-human-CD19 BUV563 1:320 SJ25C1 BD Biosciences Cat#612916 N/A
anti-human-CD56 PE/Dazzle 1:640 HDC56 BioLegend Cat#318348 RRID:AB_2563564
Anti-human CD45RO BV650 1:200 UCHL1 BioLegend Cat#304231 RRID:AB_2561359
Anti-human CD45RA BV605 1:400 HI100 BioLegend Cat#304133 RRID:AB_11126164

Immunofluorescence staining
Anti-human CD45 not-conjugated 1:100 polyclonal LSBio Cat# LS-B14248-300 RRID:AB_2889893
Anti-human CD103 not-conjugated 1:100 EPR22590-27 Abcam Cat# ab224202 RRID:AB_2891141
Anti-human CD8 not-conjugated 1:100 4B11 Bio-rad Cat# MCA1817T RRID:AB_323534
Anti-human CD3 AF647 1:50 UCHT1 BioLegend Cat# 300416 RRID:AB_389332
Anti-human CD31 not-conjugated 1:100 polyclonal R&D Systems Cat# PA5-96055 RRID: AB_2549792
Anti-human PD1 AF647 1:50 NAT105 BioLegend Cat# 367419 RRID:AB_2721353
Anti-human P2RY12 not-conjugated 1:600 polyclonal Sigma-Aldrich Cat# HPA014518 RRID:AB_2669027
Anti-human CD68 not-conjugated 1:100 KP1 Abcam Cat# ab955 RRID:AB_307338
Anti-human CD49D not-conjugated 1:100 PS/2 BioXCell Cat# BE0071 RRID:AB_1107657
Anti-human Pan-Cadherin not-conjugated 1:100 polyclonal Abcam Cat# ab16505 RRID:AB_443397
Donkey anti-goat AF488 AF488 1:500 polyclonal Invitrogen Cat# A32814 RRID:AB_2762838
Donkey anti-rabbit AF555 AF555 1:500 polyclonal Invitrogen Cat# A-32794 RRID:AB_2762834
Donkey anti-rat IgG H&L AF647 AF647 1:500 polyclonal Abcam Cat# ab150155 RRID:AB_2813835
Donkey anti-mouse IgG (H+L) AF647 AF647 1:500 polyclonal Invitrogen Cat# A-31571 RRID:AB_162542
Donkey anti-rabbit IgG (H+L) AF755 AF755 1:500 polyclonal Invitrogen Cat# SA5-10043 RRID:AB_2556623

Ex vivo treatment
Ultra-LEAF™ Purified anti-human PD1 (Mouse IgG1) not-conjugated 40ug/ml EH12.2H7 BioLegend Cat# 329926 RRID:AB_11147365
Purified Mouse IgG1, κ Isotype Ctrl not-conjugated 40ug/ml "
MG1-45" BioLegend Cat# 401401 RRID:AB_2801452

Validation

All antibodies were validated by the respective vendors. Relevant information on antibody validation can be found on the manufacturer's websites using the catalog number which is provided for each antibody used and listed in the section above.

Antibodies purchased from BioLegend for flow cytometry, immunofluorescence staining, and the functional assays were validated as followed: “Specificity testing of 1-3 target cell types with either single- or multi-color analysis (including positive and negative cell types). Once specificity is confirmed, each new lot must perform with similar intensity to the in-date reference lot. Brightness (MFI) is evaluated from both positive and negative populations. Each lot product is validated by QC testing with a series of titration dilutions.” (https://www.biolegend.com/en-us/quality/quality-control).
Antibodies purchased from BD Bioscience for flow cytometry were validated as followed: “The specificity is confirmed by using multiple applications that may include a combination of flow cytometry, immunofluorescence , immunohistochemistry or western blot to test a combination of primary cells, cell lines or transfectant models. All flow cytometry reagents are titrated on the relevant positive or negative cells.” (https://www.bdbiosciences.com/en-ch/products/reagents/flow-cytometry-reagents/research-reagents/quality-and-reproducibility).
Antibodies purchased from eBioscience/ Thermo Fisher were validated as followed: “[…] antibody has been pre-titrated and tested by flow cytometric analysis of normal human peripheral blood cells.” (https://www.thermofisher.com/ch/en/home/life-science/antibodies/invitrogen-antibody-validation.html).
Antibodies purchased from Abcam for immunofluorescence staining were validated as followed: “Antibody specificity is confirmed by looking at cells that either do or do not express the target protein within the same tissue. […] We then check the protein expression by IHC/ICC to see if it has the expected cellular localization. […] We use a variety of methods, including staining multi-normal human tissue microarrays (TMAs), multi-tumor human TMAs […]” (https://www.abcam.com/primary-antibodies/how-we-validate-our-antibodies#IHC%20and%20ICC).
Antibodies purchased from R&D Systems for immunofluorescence staining were validated as followed: “ […] We are continuously testing our products with knockout cell lines to ensure our antibodies are detecting the correct target. […]” (https://www.rndsystems.com/quality/antibodies-built-for-reproducibility).
The specificity of the anti-human P2RY12 antibody from Sigma-Aldrich was validated with the companies’ standard method and additionally with orthogonal RNAseq: “We […] test in as many additional immunodetection applications as practical in samples chosen to be relevant to the intended use of the product. These include immunohistochemistry, immunocytochemistry (ICC), Western blot, ELISA, immunoprecipitation, and more. […] What is demonstrated is a direct comparison of mRNA expression level and sample staining.” (https://www.sigmaaldrich.com/CH/en/technical-documents/technical-article/protein-biology/immunohistochemistry/antibody-enhanced-validation).

In addition to the validation by the distributors, antibodies were titrated in our lab for the use with brain tumor samples. Full-minus-one (FMO) controls were used in flow cytometry and secondary-only controls were used in immunofluorescence staining analysis. An Mouse IgG1, κ Isotype control antibody was used in the ex-vivo functional assay.

Flow Cytometry

Plots

Confirm that:

☒ The axis labels state the marker and fluorochrome used (e.g. CD4-FITC).

☒ The axis scales are clearly visible. Include numbers along axes only for bottom left plot of group (a 'group' is an analysis of identical markers).

☒ All plots are contour plots with outliers or pseudocolor plots.

☒ A numerical value for number of cells or percentage (with statistics) is provided.

Methodology

Sample preparation	Sample preparation was as described previously in (Klemm et al., 2020; Maas et al., 2021). Tissue was macrodissected and enzymatically digested with the Brain Tumor Dissociation Kit (P) for glioma samples and with the Tumor Dissociation Kit for BrM samples, both purchased from Miltenyi, and using an OctoMacs dissociator according to manufacturers instructions. Cell suspensions were filtered through a 70 µm mesh filter and, for glioma samples only, incubated with Myelin Removal Beads for 15 mins at 4 °C prior to magnetic separation by filtering through LS Columns (Miltenyi). Red blood cell lysis was performed using the RBC buffer from Biolegend according to the manufacturer's instructions. In between individual steps, samples were washed with FACS buffer (PBS + 0.5 % BSA + 2 mM EDTA) and centrifuged for 10 mins at 300 g. Dead cells were labeled by incubation with the Zombie NIR solution (BioLegend) for 10 mins at RT. Samples were subsequently incubated with Human TruStain FcX Fc receptor blocking solution (BioLegend) for 10 mins at RT, followed by antibody incubation at 4 °C, 15 mins. Samples were washed and resuspended in FACS Buffer + 1:100 EDTA (0.25 M) and kept on ice until flow cytometric analysis or sorting.
Instrument	Flow Cytometry: BD Fortessa and FACSymphony A5 FACS Sort: Aria III
Software	BD Facs Diva software. Downstream analysis with R.
Cell population abundance	Post-sort reanalyses were performed with initial sorts which revealed >90% purity of the cell populations and is illustrated in Extended Data Fig. 1b and 2a. Median fluorescence intensity (MFI) analysis was performed on samples with at least 100 cells in the analyzed population.
Gating strategy	The gating strategy for flow cytometry and cell sorting was as previously described (Klemm et al., 2020) and can additionally be found in detail in this study in Extended Data Fig. 1b, 2a, 2c, 5d and Figure 3a, 3i, 6g. FSC and SSC were used for identification of cells of interest. FSC-A, FSC-W and FSC-H were used to exclude doublets. Live/ dead cell staining was performed with Zombie NIR Fixable Viability Kit (BioLegend).

☒ Tick this box to confirm that a figure exemplifying the gating strategy is provided in the Supplementary Information.